

Condensed surfaces of magnetic neutron stars, thermal surface emission, and particle acceleration above pulsar polar caps

Zach Medin^{*} and Dong Lai[†]

Department of Astronomy, Center for Radiophysics and Space Research, Cornell University, Ithaca, NY 14853, USA

Accepted 2007 September 18. Received 2007 September 17; in original form 2007 August 28

ABSTRACT

Recent calculations indicate that the cohesive energy of condensed matter increases with magnetic field strength and becomes very significant at magnetar-like fields (e.g., 10 keV at 3×10^{14} G for zero-pressure condensed iron). This implies that for sufficiently strong magnetic fields and/or low temperatures, the neutron star surface may be in a condensed state with little gas or plasma above it. Such surface condensation can significantly affect the thermal emission from isolated neutron stars, and may lead to the formation of a charge-depleted acceleration zone (“vacuum gap”) in the magnetosphere above the stellar polar cap. Using the latest results on the cohesive property of magnetic condensed matter, we quantitatively determine the conditions for surface condensation and vacuum gap formation in magnetic neutron stars. We find that condensation can occur if the thermal energy kT of the neutron star surface is less than about 8% of its cohesive energy Q_s , and that a vacuum gap can form if $\boldsymbol{\Omega} \cdot \mathbf{B}_p < 0$ (i.e., the neutron star’s rotation axis and magnetic moment point in opposite directions) and kT is less than about 4% of Q_s . For example, at $B = 3 \times 10^{14}$ G, a condensed Fe surface forms when $T \lesssim 10^7$ K and a vacuum gap forms when $T \lesssim 5 \times 10^6$ K. Thus, vacuum gap accelerators may exist for some neutron stars. Motivated by this result, we also study the physics of pair cascades in the (Ruderman-Sutherland type) vacuum gap model for photon emission by accelerating electrons and positrons due to both curvature radiation and resonant/nonresonant inverse Compton scattering. Our calculations of the condition of cascade-induced vacuum breakdown and the related pulsar death line/boundary generalize previous works to the superstrong field regime. We find that inverse Compton scatterings do not produce a sufficient number of high energy photons in the gap (despite the fact that resonantly upscattered photons can immediately produce pairs for $B \gtrsim 1.6 \times 10^{14}$ G) and thus do not lead to pair cascades for most neutron star parameters (spin and magnetic field). We discuss the implications of our results for the recent observations of neutron star thermal radiation as well as for the detection/non-detection of radio emission from high-B pulsars and magnetars.

Key words: radiation mechanisms: non-thermal – radiation mechanisms: thermal – stars: magnetic fields – stars: neutron – pulsars: general.

1 INTRODUCTION

Recent observations of neutron stars have provided a wealth of information on these objects, but they have also raised many new questions. For example, with the advent of X-ray telescopes such as Chandra and XMM-Newton, detailed observations of the thermal radiation from the neutron star surface have become possible. These observations show that some nearby

^{*} Email: zach@astro.cornell.edu

[†] Email: dong@astro.cornell.edu

isolated neutron stars (e.g., RX J1856.5-3754) appear to have featureless, nearly blackbody spectra (Burwitz et al. 2003; van Kerkwijk & Kaplan 2007). Radiation from a bare condensed surface (where the overlying atmosphere has negligible optical depth) has been invoked to explain this nearly perfect blackbody emission (e.g., Burwitz et al. 2003; Mori & Ruderman 2003; Turolla et al. 2004; van Adelsberg et al. 2005; Perez-Azorin et al. 2006; Ho et al. 2007; but see Ruderman 2003 for an alternative view). However, whether surface condensation actually occurs depends on the cohesive properties of the surface matter (e.g., Lai 2001).

Equally puzzling are the observations of anomalous X-ray pulsars (AXPs) and soft gamma-ray repeaters (SGRs) (see Woods & Thompson 2005 for a review). Though these stars are believed to be magnetars, neutron stars with extremely strong magnetic fields ($B \gtrsim 10^{14}$ G), they mostly show no pulsed radio emission (but see Camilo et al. 2006, 2007; Kramer et al. 2007) and their X-ray radiation is too strong to be powered by rotational energy loss. By contrast, several high-B radio pulsars with inferred surface field strengths similar to those of magnetars have been discovered (e.g., Kaspi & McLaughlin 2005; Vranevsevic, Manchester, & Melrose 2007). A deeper understanding of the distinction between pulsars and magnetars requires further investigation of the mechanisms by which pulsars and magnetars radiate and of their magnetospheres where this emission originates. Theoretical models of pulsar and magnetar magnetospheres depend on the cohesive properties of the surface matter in strong magnetic fields (e.g., Ruderman & Sutherland 1975; Arons & Scharlemann 1979; Cheng & Ruderman 1980; Usov & Melrose 1996; Harding & Muslimov 1998; Gil, Melikidze, & Geppert 2003; Muslimov & Harding 2003; Beloborodov & Thompson 2007). For example, depending on how strongly bound the surface matter is, a charge-depleted acceleration zone (“vacuum gap”) above the polar cap of a pulsar may or may not form, and this will affect pulsar radio emission and other high-energy emission processes.

The cohesive property of the neutron star surface matter plays a key role in these and other neutron star processes and observed phenomena. The cohesive energy refers to the energy required to pull an atom out of the bulk condensed matter at zero pressure. A related (but distinct) quantity is the electron work function, the energy required to pull out an electron. For magnetized neutron star surfaces the cohesive energy and work function can be many times the corresponding terrestrial values, due to the strong magnetic fields threading the matter (e.g., Ruderman 1974; Lai 2001).

In two recent papers (Medin & Lai 2006a,b, hereafter ML06a,b), we carried out detailed, first-principle calculations of the cohesive properties of H, He, C, and Fe surfaces at field strengths between $B = 10^{12}$ G to 2×10^{15} G. The main purpose of this paper is to investigate several important astrophysical implications of these results (some preliminary investigations were reported in Medin & Lai 2007). This paper is organized as follows. In Section 2 we briefly summarize the key results (cohesive energy and work function values) of ML06a,b used in this paper. In Section 3 we examine the possible formation of a bare neutron star surface, which directly affects the surface thermal emission. We find that the critical temperature below which a phase transition to the condensed state occurs is approximately given by $kT_{\text{crit}} \sim 0.08Q_s$, where Q_s is the cohesive energy of the surface. In Section 4 we consider the conditions for the formation of a polar vacuum gap in pulsars and magnetars. We find that neutron stars with rotation axis and magnetic moment given by $\boldsymbol{\Omega} \cdot \mathbf{B}_p > 0$ are unable to form vacuum gaps (since the electrons which are required to fill the gaps can be easily supplied by the surface), but neutron stars with $\boldsymbol{\Omega} \cdot \mathbf{B}_p < 0$ can form vacuum gaps provided that the surface temperature is less than $kT_{\text{crit}} \sim 0.04Q_s$ (and that particle bombardment does not completely destroy the gap; see Section 6). In Section 5 we discuss polar gap radiation mechanisms and the pulsar death line/boundary in the vacuum gap model. We find that when curvature radiation is the dominant radiation mechanism in the gap, a pair cascade is possible for a large range of parameter space (in the $P-\dot{P}$ diagram), but when inverse Compton scattering (either resonant or nonresonant) is the dominant radiation mechanism, vacuum breakdown is possible for only a very small range of parameter values. Implications of our results for recent observations are discussed in Section 6. Some technical details (on our treatment of inverse Compton scattering and vacuum gap electrodynamics of oblique rotators) are given in two appendices.

2 COHESIVE PROPERTIES OF CONDENSED MATTER IN STRONG MAGNETIC FIELDS

It is well-known that the properties of matter can be drastically modified by strong magnetic fields. The natural atomic unit for the magnetic field strength, B_0 , is set by equating the electron cyclotron energy $\hbar\omega_{ce} = \hbar(eB/m_e c) = 11.577 B_{12}$ keV, where $B_{12} = B/(10^{12}$ G), to the characteristic atomic energy $e^2/a_0 = 2 \times 13.6$ eV (where a_0 is the Bohr radius):

$$B_0 = \frac{m_e^2 e^3 c}{\hbar^3} = 2.3505 \times 10^9 \text{ G}. \quad (1)$$

For $b = B/B_0 \gtrsim 1$, the usual perturbative treatment of the magnetic effects on matter (e.g., Zeeman splitting of atomic energy levels) does not apply. Instead, the Coulomb forces act as a perturbation to the magnetic forces, and the electrons in an atom settle into the ground Landau level. Because of the extreme confinement of the electrons in the transverse direction (perpendicular to the field), the Coulomb force becomes much more effective in binding the electrons along the magnetic field direction. The atom attains a cylindrical structure. Moreover, it is possible for these elongated atoms to form molecular

chains by covalent bonding along the field direction. Interactions between the linear chains can then lead to the formation of three-dimensional condensed matter (Ruderman 1974; Ruder et al. 1994; Lai 2001).

The basic properties of magnetized condensed matter can be estimated using the uniform electron gas model (e.g., Kadomtsev 1970). The energy per cell of a zero-pressure condensed matter is given by

$$\mathcal{E}_s \sim -120 Z^{9/5} B_{12}^{2/5} \text{ eV}, \quad (2)$$

and the corresponding condensation density is

$$\rho_s \sim 560 A Z^{-3/5} B_{12}^{6/5} \text{ g cm}^{-3}, \quad (3)$$

where Z , A are the charge number and mass number of the ion (see Lai 2001 and references therein for further refinements to the uniform gas model). Although this simple model gives a reasonable estimate of the binding energy for the condensed state, it is not adequate for determining the cohesive property of the condensed matter. The cohesive energy is the (relatively small) difference between the atomic ground-state energy \mathcal{E}_a and the zero-pressure condensed matter energy \mathcal{E}_s , both increasing rapidly with B . Moreover, the electron Fermi energy (including both kinetic energy and Coulomb energy) in the uniform gas model,

$$\varepsilon_F = (3/5Z)\mathcal{E}_s \sim -73Z^{4/5} B_{12}^{2/5} \text{ eV}, \quad (4)$$

may not give a good scaling relation for the electron work function when detailed electron energy levels (bands) in the condensed matter are taken into account.

There have been few quantitative studies of infinite chains and zero-pressure condensed matter in strong magnetic fields. Earlier variational calculations (e.g., Flowers et al. 1977; Müller 1984) as well as calculations based on Thomas-Fermi type statistical models (e.g., Abrahams & Shapiro 1991; Fushiki et al. 1992), while useful in establishing scaling relations and providing approximate energies of the atoms and the condensed matter, are not adequate for obtaining reliable energy differences (cohesive energies). Quantitative results for the energies of infinite chains of hydrogen molecules H_∞ over a wide range of field strengths ($B \gg B_0$) were presented in Lai et al. (1992) (using the Hartree-Fock method with the plane-wave approximation; see also Lai 2001 for some results for He_∞) and in Relovsky & Ruder (1996) (using density functional theory). For heavier elements such as C and Fe, the cohesive energies of one dimensional (1D) chains have only been calculated at a few magnetic field strengths in the range of $B = 10^{12}$ – 10^{13} G, using Hartree-Fock models (Neuhauser et al. 1987) and density functional theory (Jones 1985). There were some discrepancies between the results of these works, and some adopted a crude treatment for the band structure (Neuhauser et al. 1987). An approximate calculation of 3D condensed matter based on density functional theory was presented in Jones (1986).

Our calculations of atoms and small molecules (ML06a) and of infinite chains and condensed matter (ML06b) are based on a newly developed density functional theory code. Although the Hartree-Fock method is expected to be highly accurate in the strong field regime, it becomes increasingly impractical for many-electron systems as the magnetic field increases, since more and more Landau orbitals are occupied (even though electrons remain in the ground Landau level) and keeping track of the direct and exchange interactions between electrons in various orbitals becomes computational rather tedious. Compared to previous density-functional theory calculations, we used an improved exchange-correlation function for highly magnetized electron gases, and we calibrated our density-functional code with previous results (when available) based on other methods. Most importantly, in our calculations of 1D condensed matter, we treated the band structure of electrons in different Landau orbitals self-consistently without adopting ad-hoc simplifications. This is important for obtaining reliable results for the condensed matter. Since each Landau orbital has its own energy band, the number of bands that need to be calculated increases with Z and B , making the computation increasingly complex for superstrong magnetic field strengths (e.g., the number of occupied bands for Fe chains at $B = 2 \times 10^{15}$ G reaches 155; see Fig. 16 of ML06b). Our density-functional calculations allow us to obtain the energies of atoms and small molecules and the energy of condensed matter using the same method, thus providing reliable cohesive energy and work function values for condensed surfaces of magnetic neutron stars.

In ML06a, we described our calculations for various atoms and molecules in magnetic fields ranging from 10^{12} G to 2×10^{15} G for H, He, C, and Fe, representative of the most likely neutron star surface compositions. Numerical results of the ground-state energies are given for H_N (up to $N = 10$), He_N (up to $N = 8$), C_N (up to $N = 5$), and Fe_N (up to $N = 3$), as well as for various ionized atoms. In ML06b, we described our calculations for infinite chains for H, He, C, and Fe in that same magnetic field range. For relatively low field strengths, chain-chain interactions play an important role in the cohesion of three-dimensional (3D) condensed matter. An approximate calculation of 3D condensed matter is also presented in ML06b. Numerical results of the ground-state and cohesive energies, as well as the electron work function and the zero-pressure condensed matter density, are given in ML06b for H_∞ and H(3D), He_∞ and He(3D), C_∞ and C(3D), and Fe_∞ and Fe(3D).

Some numerical results from ML06a,b are provided in graphical form in Figs. 1, 2, 3, and 4 (see ML06a,b for approximate scaling relations for different field ranges based on numerical fits). Figure 1 shows the cohesive energies of condensed matter, $Q_s = \mathcal{E}_1 - \mathcal{E}_s$, and the molecular energy differences, $\Delta\mathcal{E}_N = \mathcal{E}_N/N - \mathcal{E}_1$, for He, Fig. 2 for C, and Fig. 3 for Fe; here \mathcal{E}_1 is the atomic ground-state energy, \mathcal{E}_N is the ground-state energy of the He_N , C_N , or Fe_N molecule, and \mathcal{E}_s is the energy per cell

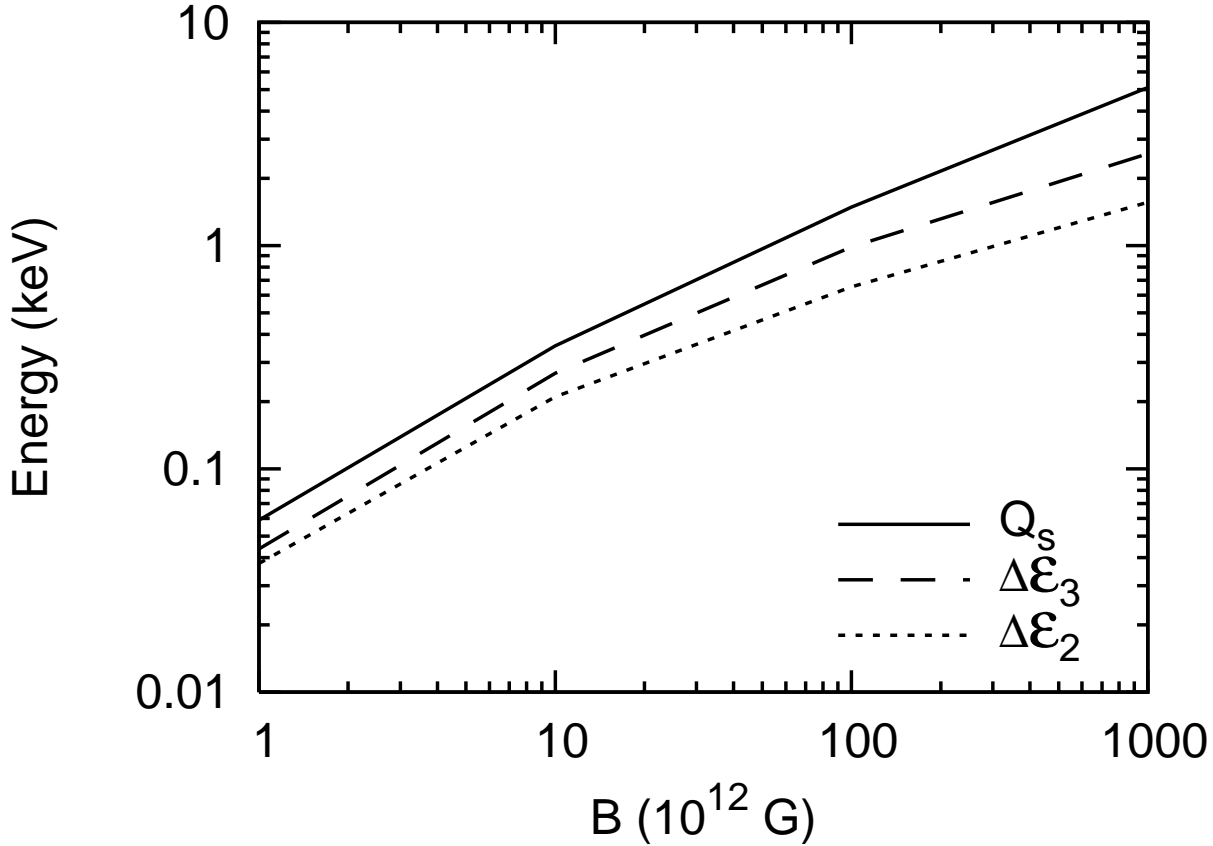


Figure 1. Cohesive energy $Q_s = \mathcal{E}_1 - \mathcal{E}_s$ and molecular energy difference $\Delta\mathcal{E}_N = \mathcal{E}_N/N - \mathcal{E}_1$ for helium as a function of the magnetic field strength.

of the zero-pressure 3D condensed matter. Some relevant ionization energies for the atoms are also shown. Figure 4 shows the electron work functions ϕ for condensed He, C, and Fe as a function of the field strength. We see that the work function increases much more slowly with B compared to the simple free electron gas model [see Eq. (4)], and the dependence on Z is also weak. The results summarized here will be used in Section 3 and Section 4 below.

3 CONDENSATION OF NEUTRON STAR SURFACES IN STRONG MAGNETIC FIELDS

As seen from Figs. 1, 2, and 3, the cohesive energies of condensed matter increase with magnetic field. We therefore expect that for sufficiently strong magnetic fields, there exists a critical temperature T_{crit} below which a first-order phase transition occurs between the condensate and the gaseous vapor. This has been investigated in detail for hydrogen surfaces (see Lai & Salpeter 1997; Lai 2001), but not for other surface compositions. Here we consider the possibilities of such phase transitions of He, C, and Fe surfaces.

A precise calculation of the critical temperature T_{crit} is difficult. We can determine T_{crit} approximately by considering the equilibrium between the condensed phase (labeled “s”) and the gaseous phase (labeled “g”) in the ultrahigh field regime (where phase separation exists). The gaseous phase consists of a mixture of free electrons and bound ions, atoms, and molecules. Phase equilibrium requires the temperature, pressure and the chemical potentials of different species to satisfy the conditions (here we consider Fe as an example; He and C are similar)

$$P_s = P_g = [2n(\text{Fe}^+) + 3n(\text{Fe}^{2+}) + \dots + n(\text{Fe}) + n(\text{Fe}_2) + n(\text{Fe}_3) + \dots]kT, \quad (5)$$

$$\mu_s = \mu_e + \mu(\text{Fe}^+) = 2\mu_e + \mu(\text{Fe}^{2+}) = \dots = \mu(\text{Fe}) = \frac{1}{2}\mu(\text{Fe}_2) = \frac{1}{3}\mu(\text{Fe}_3) = \dots, \quad (6)$$

where we treat the gaseous phase as an ideal gas. The chemical potential of the condensed phase is given by

$$\mu_s = \mathcal{E}_s + P_s V_s \simeq \mathcal{E}_{s,0}, \quad (7)$$

where \mathcal{E}_s is the energy per cell of the condensate and $\mathcal{E}_{s,0}$ is the energy per cell at zero-pressure (we will label this simply as

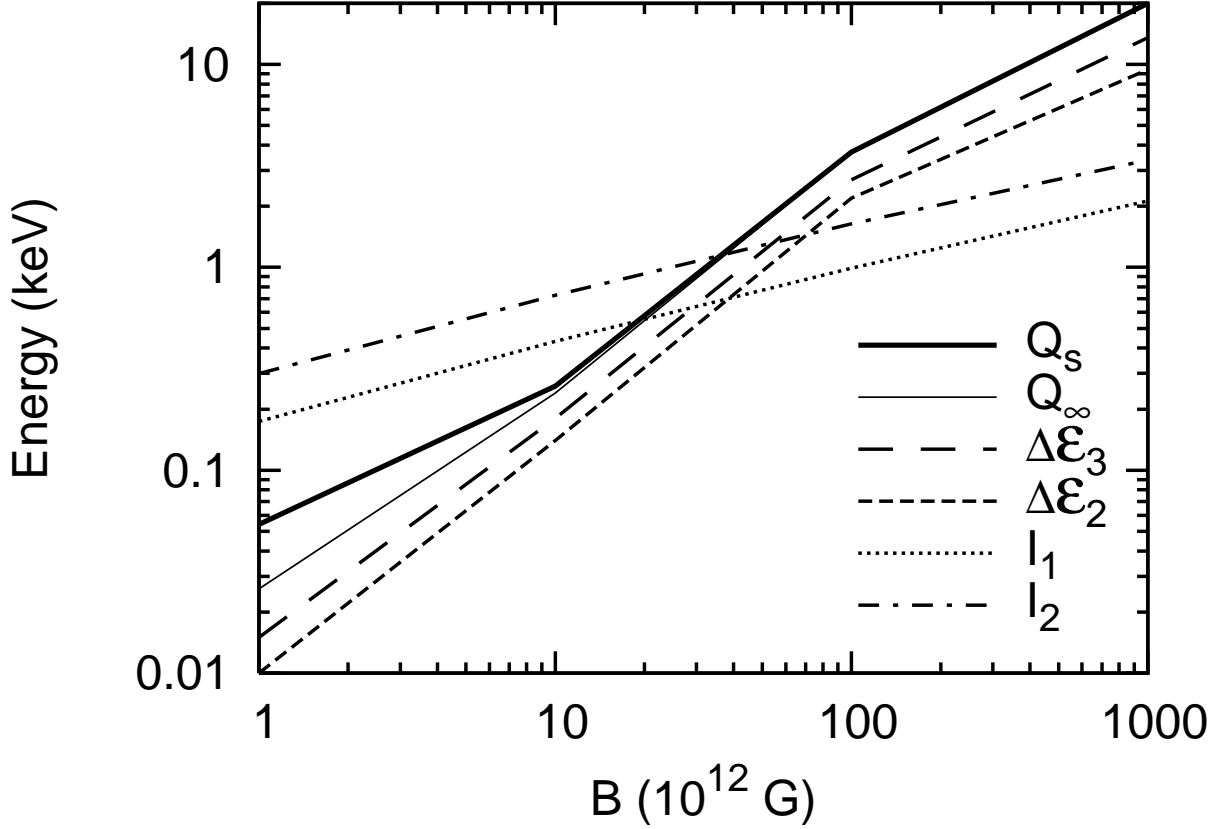


Figure 2. Cohesive energy $Q_s = \mathcal{E}_1 - \mathcal{E}_s$ and molecular energy difference $\Delta\mathcal{E}_N = \mathcal{E}_N/N - \mathcal{E}_1$ for carbon as a function of the magnetic field strength. The symbol Q_∞ represents the cohesive energy of a one-dimensional chain, and I_1 and I_2 are the first and second ionization energies of the C atom.

\mathcal{E}_s). We have assumed that the vapor pressure is sufficiently small so that the deviation from the zero-pressure state of the condensate is small; this is justified when the saturation vapor pressure P_{sat} is much less than the critical pressure P_{crit} for phase separation, or when the temperature is less than the critical temperature by a factor of a few.

For nondegenerate electrons in a strong magnetic field the number density is related to μ_e by

$$n_e \simeq \frac{1}{2\pi\rho_0^2} e^{\mu_e/kT} \sum_{n_L=0}^{\infty} g_{n_L} \exp\left(\frac{-n_L \hbar\omega_{ce}}{kT}\right) \int_{-\infty}^{\infty} \frac{dp_z}{h} \exp\left(\frac{-p_z^2}{2m_e kT}\right) \quad (8)$$

$$\simeq \frac{1}{2\pi\rho_0^2 \lambda_{Te}} e^{\mu_e/kT} \tanh^{-1}\left(\frac{\hbar\omega_{ce}}{2kT}\right) \quad (9)$$

$$\simeq \frac{1}{2\pi\rho_0^2 \lambda_{Te}} e^{\mu_e/kT}, \quad (10)$$

where $g_{n_L} = 1$ for $n_L = 0$ and $g_{n_L} = 2$ for $n_L > 0$ are the Landau degeneracies, $\lambda_{Te} = (2\pi\hbar^2/m_e kT)^{1/2}$ is the electron thermal wavelength, and the last equality applies for $kT \ll \hbar\omega_{ce}$. The magnetic field length is $\rho_0 = (\hbar c/eB)^{1/2}$. For atomic, ionic, or molecular Fe the number density is given by

$$n(\text{Fe}_A) \simeq \frac{1}{h^3} e^{\mu_A/kT} \sum_i \exp\left(-\frac{\mathcal{E}_{A,i}}{kT}\right) \int d^3K \exp\left(\frac{-K^2}{2M_A kT}\right) \quad (11)$$

$$\simeq \frac{1}{\lambda_{TA}^3} \exp\left(-\frac{\mathcal{E}_A - \mu_A}{kT}\right) Z_{\text{int}}(\text{Fe}_A), \quad (12)$$

with the internal partition function

$$Z_{\text{int}}(\text{Fe}_A) = \sum_i \exp\left(-\frac{\Delta\mathcal{E}_{A,i}}{kT}\right). \quad (13)$$

and $\Delta\mathcal{E}_{A,i} = \mathcal{E}_{A,i} - \mathcal{E}_A$. Here, the subscript A represents the atomic, ionic, or molecular species whose number density we are

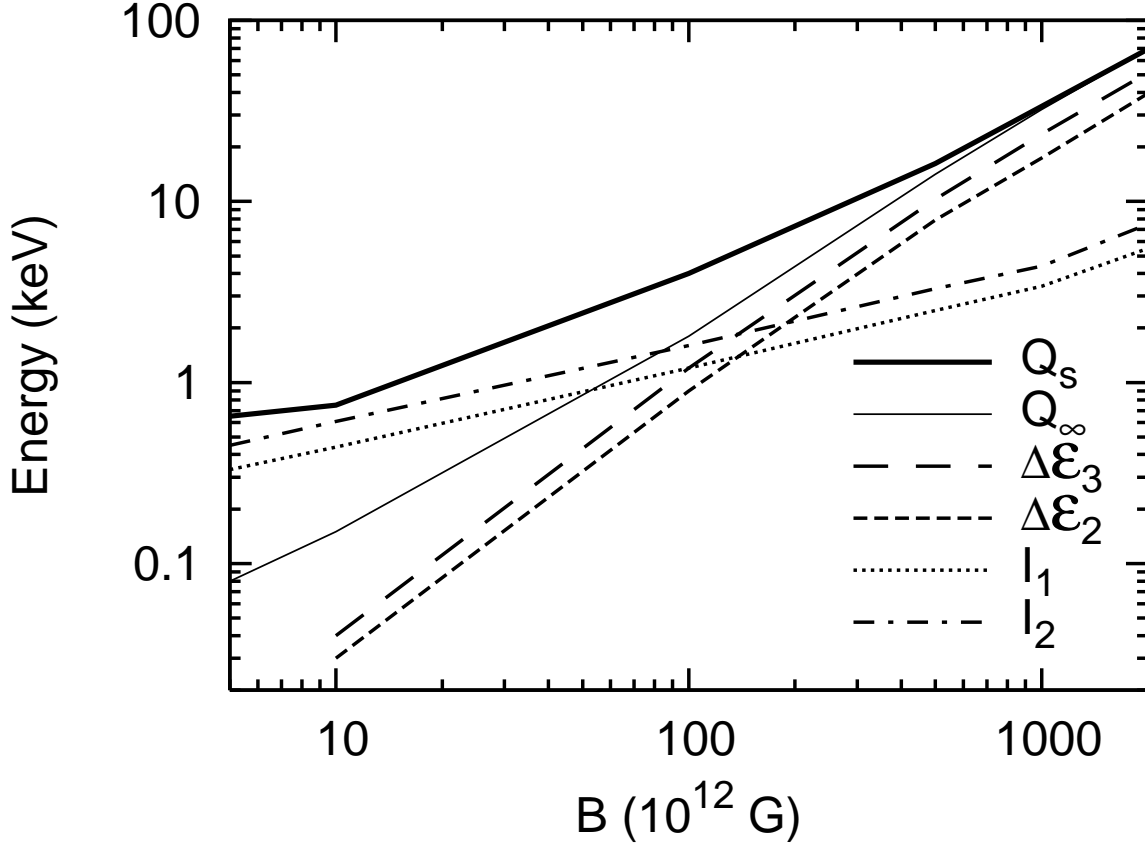


Figure 3. Cohesive energy $Q_s = \mathcal{E}_1 - \mathcal{E}_s$ and molecular energy difference $\Delta\mathcal{E}_N = \mathcal{E}_N/N - \mathcal{E}_1$ for iron as a function of the magnetic field strength. The symbol Q_∞ represents the cohesive energy of a one-dimensional chain, and I_1 and I_2 are the first and second ionization energies of the Fe atom. Below 5×10^{12} G, our results for Q_∞ and Q_s become unreliable as Q_∞ and Q_s become very small and approach numerical errors for \mathcal{E}_N and \mathcal{E}_s .

calculating (e.g., Fe_2 or Fe^+) and the sum \sum_i is over all excited states of that species. Also, $\lambda_{Te} = (2\pi\hbar^2/M_A kT)^{1/2}$ is the Fe particle’s thermal wavelength, where $M_A = NAM$ is the total mass of the particle (N is the number of “atoms” in the molecule, A is the atomic mass number, and $M = m_p + m_e$). The vector \mathbf{K} represents the center-of-mass momentum of the particle. Note that we have assumed here that the Fe_A particle moves across the field freely; this is a good approximation for large M_A . The internal partition function Z_{int} represents the effect of all excited states of the species on the total density; in this work we will use the approximation that this factor is the same for all species, and we will estimate the magnitude of this factor later in this section.

The equilibrium condition $\mu_s = \mu(\text{Fe})$ for the process $\text{Fe}_{s,\infty} + \text{Fe} = \text{Fe}_{s,\infty+1}$ yields the atomic density in the saturated vapor:

$$n(\text{Fe}) \simeq \left(\frac{AMkT}{2\pi\hbar^2} \right)^{3/2} \exp\left(-\frac{Q_s}{kT}\right) Z_{\text{int}}, \quad (14)$$

where $Q_s = \mathcal{E}_1 - \mathcal{E}_s$ is the cohesive energy of the condensed Fe. The condition $N\mu_s = \mu(\text{Fe}_N)$ for the process $\text{Fe}_{s,\infty} + \text{Fe}_N = \text{Fe}_{s,\infty+N}$ yields the molecular density in the vapor:

$$n(\text{Fe}_N) \simeq \left(\frac{NAMkT}{2\pi\hbar^2} \right)^{3/2} \exp\left(-\frac{S_N}{kT}\right) Z_{\text{int}}, \quad (15)$$

where

$$S_N = \mathcal{E}_N - N\mathcal{E}_s = N[Q_s - (\mathcal{E}_1 - \mathcal{E}_N/N)] \quad (16)$$

is the “surface energy” and \mathcal{E}_N/N is the energy per ion in the molecule. The equilibrium condition $\mu(\text{Fe}^{n+}) = \mu_e + \mu(\text{Fe}^{(n+1)+})$ for the process $e + \text{Fe}^{n+} = \text{Fe}^{(n+1)+}$, where Fe^{n+} is the n th ionized state of Fe, yields the vapor densities for the ions:

$$n(\text{Fe}^+)n_e \simeq \frac{b}{2\pi a_0^2} \sqrt{\frac{m_e kT}{2\pi\hbar^2}} \exp\left(-\frac{I_1}{kT}\right) n(\text{Fe}), \quad (17)$$

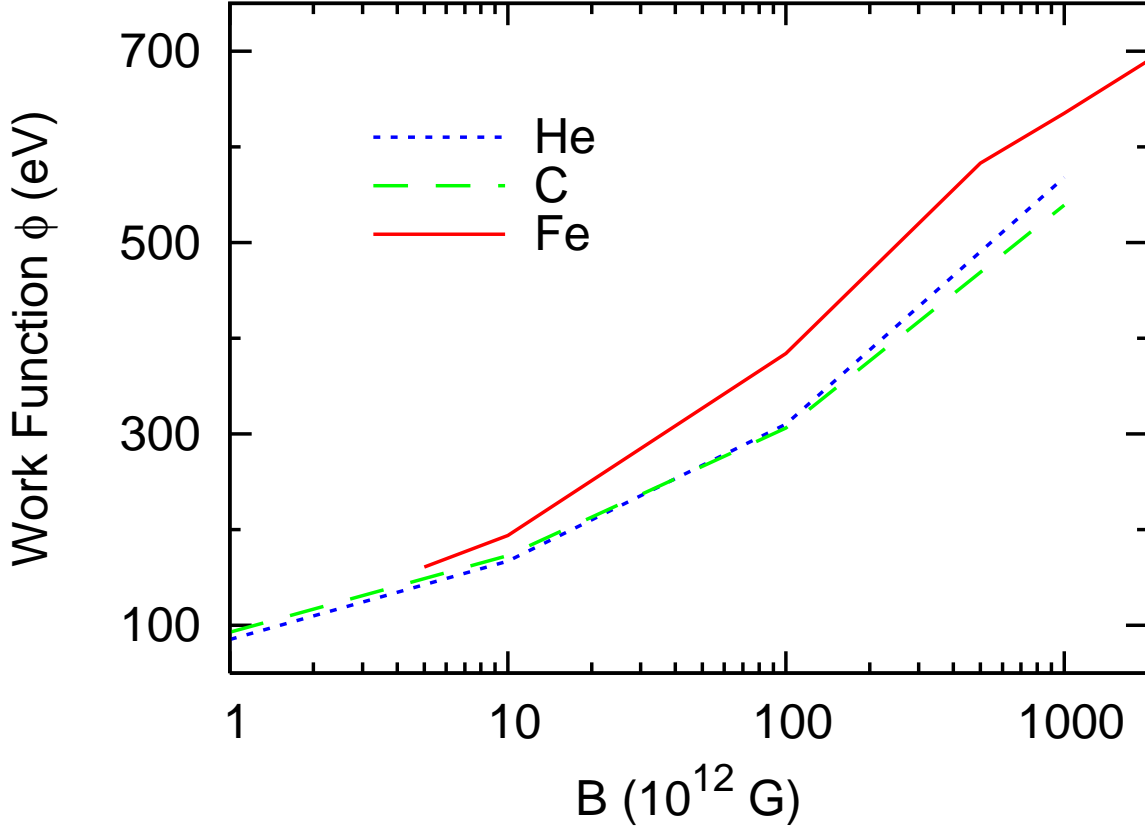


Figure 4. Numerical result for the electron work function as a function of the magnetic field strength, for He, C, and Fe infinite chains.

$$n(\text{Fe}^{2+})n_e \simeq \frac{b}{2\pi a_0^2} \sqrt{\frac{m_e kT}{2\pi \hbar^2}} \exp\left(-\frac{I_2}{kT}\right) n(\text{Fe}^+), \quad (18)$$

and so on. Here, $b = B/B_0$ and a_0 is the Bohr radius, and $I_n = \mathcal{E}_{(n-1)+} - \mathcal{E}_{n+}$ represents the ionization energy of the n th ionized state of Fe (i.e., the amount of energy required to remove the n th electron from the atom when the first $n-1$ electrons have already been removed). The total electron density in the saturated vapor is

$$n_e = n(\text{Fe}^+) + 2n(\text{Fe}^{2+}) + \dots. \quad (19)$$

The number densities of electrons [Eq. (19)] and ions [e.g., Eqs. (17) and (18)] must be found self-consistently, for all ion species that contribute significantly to the total vapor density. The total mass density in the vapor is calculated from the number densities of all of the species discussed above, using the formula

$$\rho_g = AM [n(\text{Fe}) + 2n(\text{Fe}_2) + \dots + n(\text{Fe}^+) + n(\text{Fe}^{2+}) + \dots]. \quad (20)$$

Figure 5 (for Fe) and Fig. 6 (for C) show the the densities of different atomic/molecular species in the saturated vapor in phase equilibrium with the condensed matter for different temperatures and field strengths. These are computed using the values of \mathcal{E}_N/N , \mathcal{E}_s , and \mathcal{E}_{n+} presented in ML06a,b and depicted in Figs. 2 and 3. As expected, for sufficiently low temperatures, the total gas density in the vapor is much smaller than the condensation density, and thus phase separation is achieved. The critical temperature T_{crit} , below which phase separation between the condensate and the gaseous vapor occurs, is determined by the condition $\rho_s = \rho_g$. We find that for Fe:

$$T_{\text{crit}} \simeq 6 \times 10^5, 7 \times 10^5, 3 \times 10^6, 10^7, 2 \times 10^7 \text{ K} \quad \text{for } B_{12} = 5, 10, 100, 500, 1000, \quad (21)$$

for C:

$$T_{\text{crit}} \simeq 9 \times 10^4, 3 \times 10^5, 3 \times 10^6, 2 \times 10^7 \text{ K} \quad \text{for } B_{12} = 1, 10, 100, 1000. \quad (22)$$

and for He:

$$T_{\text{crit}} \simeq 8 \times 10^4, 3 \times 10^5, 2 \times 10^6, 9 \times 10^6 \text{ K} \quad \text{for } B_{12} = 1, 10, 100, 1000. \quad (23)$$

In terms of the cohesive energy, these results can be approximated by

$$kT_{\text{crit}} \sim 0.08 Q_s. \quad (24)$$

Note that in our calculations for the iron vapor density at $B_{12} = 5\text{-}500$ we have estimated the magnitude of the internal partition function factor Z_{int} ; the modified total density curves are marked on these figures as “ $\rho_g \times Z_{\text{int}}$ ”. To estimate Z_{int} we use Eq. (13) with a cutoff to the summation above some energy. For $B_{12} = 5, 10, 100,$ and 500 we calculate or interpolate the energies for all excited states of atomic Fe with energy below this cutoff, in order to find Z_{int} . The energy cutoff is necessary because the highly excited states become unbound (ionized) due to finite pressure and should not be included in Z_{int} (otherwise Z_{int} would diverge). In principle, the cutoff is determined by requiring the effective size of the excited state to be smaller than the inter-particle space in the gas, which in turn depends on density. In practice, we choose the cutoff such that the highest excited state has a binding energy $|\mathcal{E}_{A,i}|$ significantly smaller than the ground-state binding energy $|\mathcal{E}_A|$ (typically 30% of it). As an approximation, we also assume that the internal partitions for Fe_N molecules and ions have the same Z_{int} as the Fe atom. Despite the crudeness of our calculation of Z_{int} , we see from Fig. 5 that the resulting T_{crit} is only reduced by a few tens of a percent from the T_{crit} value assuming $Z_{\text{int}} = 1$.

We note that our calculation of the saturated vapor density is very uncertain around $T \sim T_{\text{crit}}$, since Eqs. (14)–(18) are derived for $\rho_g \ll \rho_s$ while the critical temperature of the saturated vapor density is found by setting $\rho_s = \rho_g$. However, since the vapor density decreases rapidly as T decreases, when the temperature is below $T_{\text{crit}}/2$ (for example), the vapor density becomes much less than the condensation density and phase transition is unavoidable. When the temperature drops below a fraction of T_{crit} , the vapor density becomes so low that the optical depth of the vapor is negligible and the outermost layer of the neutron star then consists of condensed matter. The radiative properties of such condensed phase surfaces have been studied using a simplified treatment of the condensed matter (see van Adelsberg et al. 2005 and references therein).

4 POLAR VACUUM GAP ACCELERATORS IN PULSARS AND MAGNETARS

A rotating, magnetized neutron star is surrounded by a magnetosphere filled with plasma. The plasma is assumed to be an excellent conductor, such that the charged particles move to screen out any electric field parallel to the local magnetic field. The corresponding charge density is given by (Goldreich & Julian 1969)

$$\rho_{GJ} \simeq -\frac{\mathbf{\Omega} \cdot \mathbf{B}}{2\pi c} \quad (25)$$

where $\mathbf{\Omega}$ is the rotation rate of the neutron star.

The Goldreich-Julian density assumes that charged particles are always available. This may not be satisfied everywhere in the magnetosphere. In particular, charged particles traveling outward along the open field lines originating from the polar cap region of the neutron star will escape beyond the light cylinder. To maintain the required magnetosphere charge density these particles have to be replenished by the stellar surface. If the surface temperature and cohesive strength are such that the required particles are tightly bound to the stellar surface, those regions of the polar cap through which the charged particles are escaping will not be replenished. A vacuum gap will then develop just above the polar cap (e.g., Ruderman & Sutherland 1975; Cheng & Ruderman 1980; Usov & Melrose 1996; Zhang, Harding, & Muslimov 2000; Gil, Melikidze, & Geppert 2003). In this vacuum gap zone the parallel electric field is no longer screened and particles are accelerated across the gap until vacuum breakdown (via pair cascade) shorts out the gap. Such an acceleration region can have an important effect on neutron star emission processes. We note that in the absence of a vacuum gap, a polar gap acceleration zone based on space-charge-limited flow may still develop (e.g., Arons & Scharlemann 1979; Harding & Muslimov 1998; Muslimov & Harding 2003).

In this section we determine the conditions required for the vacuum gap to exist using our results summarized in Section 2. The cohesive energy and electron work function of the condensed neutron star surface are obviously the key factors. We examine the physics of particle emission from condensed surface in more detail than considered previously.

4.1 Particle Emission From Condensed Neutron Star Surfaces

We assume that the NS surface is in the condensed state, i.e., the surface temperature T is less than the critical temperature T_{crit} for phase separation (see Section 3). (If $T > T_{\text{crit}}$, the surface will be in gaseous phase and a vacuum gap will not form.) We shall see that in order for the surface not to emit too large a flux of charges to the magnetosphere (a necessary condition for the vacuum gap to exist), an even lower surface temperature will be required.

4.1.1 Electron Emission

For neutron stars with $\mathbf{\Omega} \cdot \mathbf{B}_p > 0$, where \mathbf{B}_p is the magnetic field at the polar cap, the Goldreich-Julian charge density is negative at the polar cap, thus surface electron emission (often called thermionic emission in solid state physics; Ashcroft & Mermin

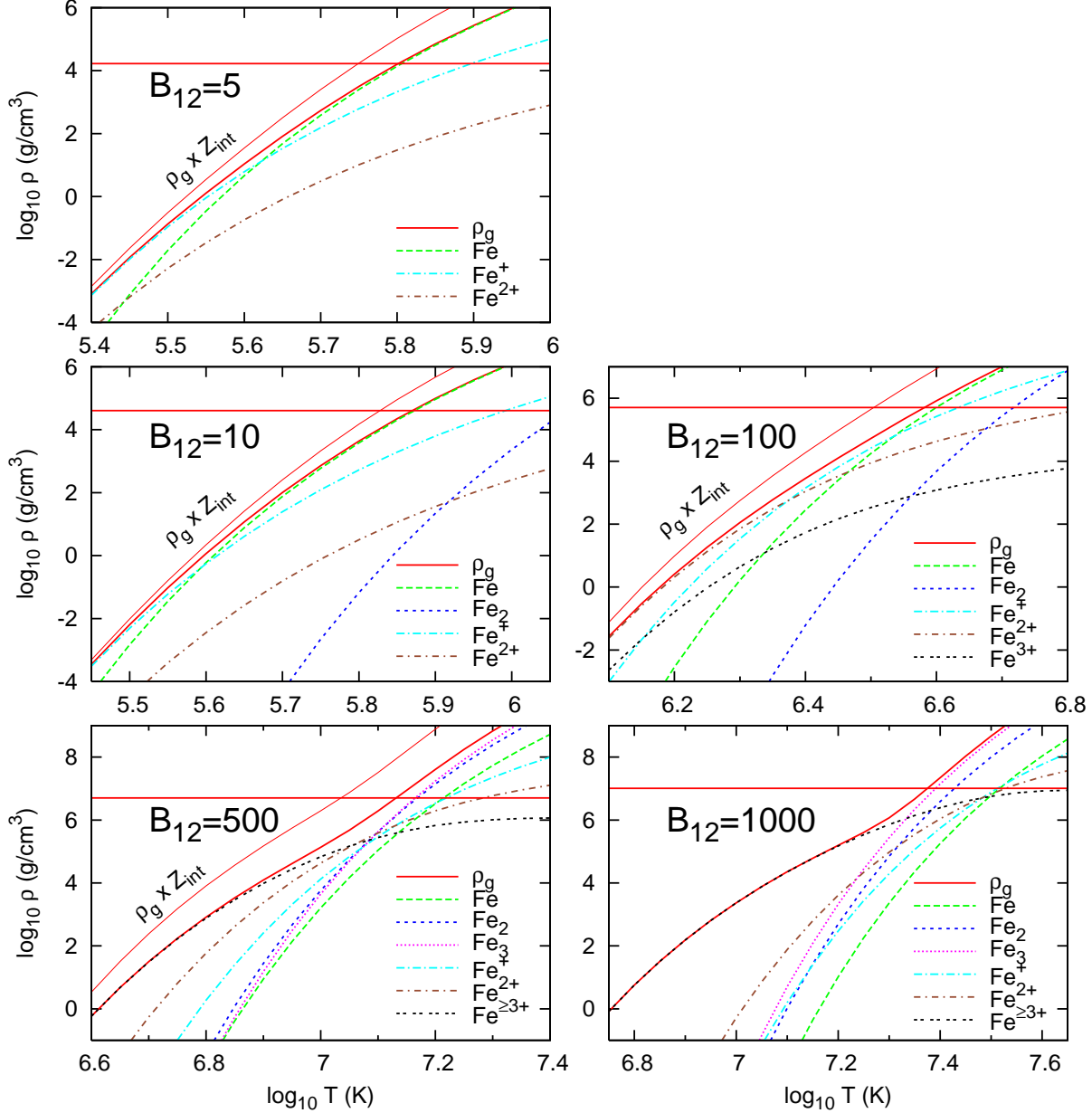


Figure 5. The mass densities of various atomic/ionic/molecular species and the total density (ρ_g) of the vapor in phase equilibrium with the condensed iron surface. The five panels are for different field strengths, $B_{12} = 5, 10, 100, 500, 1000$. The horizontal lines give the densities of the condensed phase, ρ_s . All the vapor density curves are calculated assuming $Z_{\text{int}} = 1$, except for the curve marked by “ $\rho_g \times Z_{\text{int}}$ ”, for which the total vapor density is calculated taking into account the nontrivial internal partition functions of various species. The critical temperature T_{crit} for phase separation is set by the condition $\rho_g = \rho_s$.

1976) is relevant. Let \mathcal{F}_e be the number flux of electrons emitted from the neutron star surface. The emitted electrons are accelerated to relativistic speed quickly, and thus the steady-state charge density is $\rho_e = -e\mathcal{F}_e/c$. For the vacuum gap to exist, we require $|\rho_e| < |\rho_{\text{GJ}}|$. (If $|e\mathcal{F}_e/c| > |\rho_{\text{GJ}}|$, the charges will be rearranged so that the charge density equals ρ_{GJ} .)

To calculate the electron emission flux from the condensed surface, we assume that these electrons behave like a free electron gas in a metal, where the energy barrier they must overcome is the work function of the metal. In a strong magnetic field, the electron flux is given by

$$\mathcal{F}_e = \int_{p_{\text{min}}}^{\infty} f(\epsilon) \frac{p_z}{m_e} \frac{1}{2\pi\rho_0^2} \frac{dp_z}{h}, \quad (26)$$

where $p_{\text{min}} = \sqrt{2m_e|U_0|}$, U_0 is the potential energy of the electrons in the metal, $\epsilon = p_z^2/(2m_e)$ is the electron kinetic energy, and

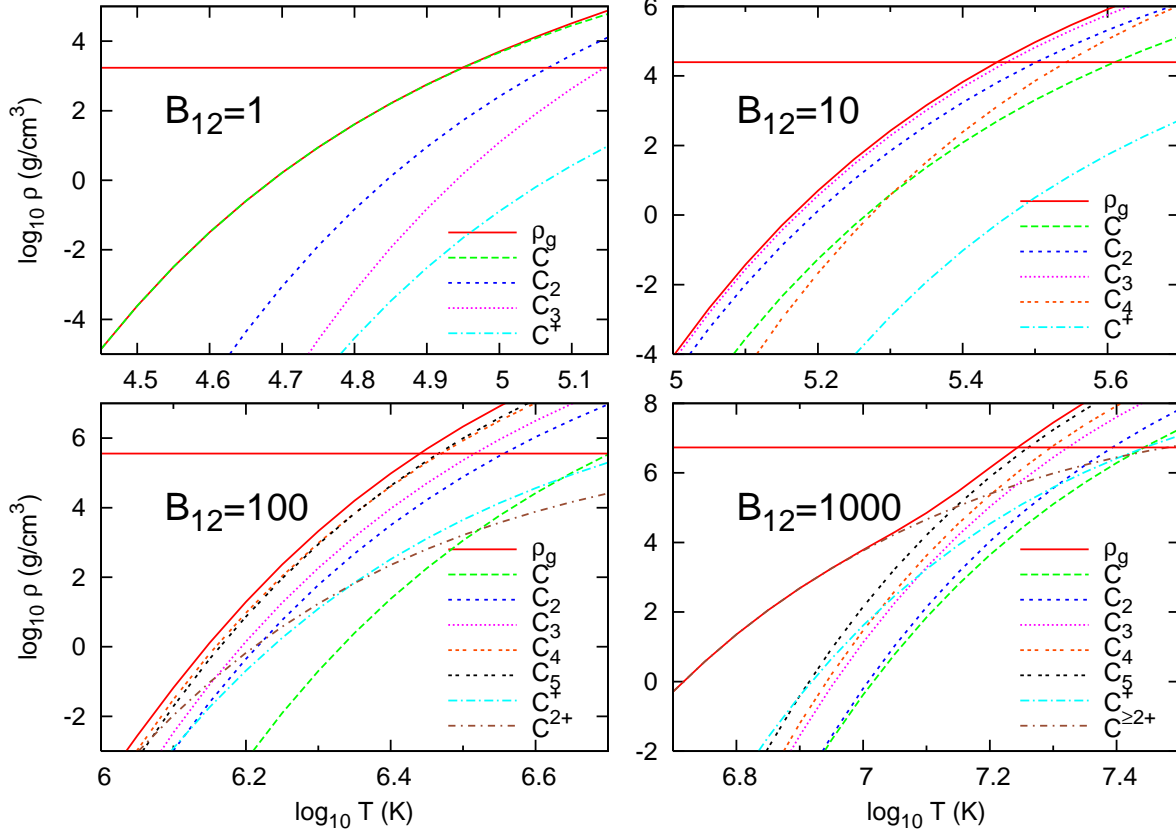


Figure 6. The mass densities of various atomic/ionic/molecular species and the total density (ρ_g) of the vapor in phase equilibrium with the condensed carbon surface. The four panels are for different field strengths, $B_{12} = 1, 10, 100, 1000$. The horizontal lines give the densities of the condensed phase, ρ_s . All the vapor density curves are calculated assuming $Z_{\text{int}} = 1$. The critical temperature T_{crit} for phase separation is set by the condition $\rho_g = \rho_s$.

$$f(\epsilon) = \frac{1}{e^{(\epsilon - \mu'_e)/kT} + 1} \quad (27)$$

is the Fermi-Dirac distribution function with μ'_e the electron chemical potential (excluding potential energy). Integrating this expression gives

$$\mathcal{F}_e = \frac{kT}{2\pi h \rho_0^2} \ln [1 + e^{-\phi/kT}] \simeq \frac{kT}{2\pi h \rho_0^2} e^{-\phi/kT}, \quad (28)$$

where $\phi \equiv |U_0| - \mu'_e$ is the work function of the condensed matter and the second equality assumes $\phi \gg kT$. The steady-state charge density supplied by the surface is then

$$\rho_e = -\frac{e}{c} \mathcal{F}_e = \rho_{GJ} \exp(C_e - \phi/kT), \quad (29)$$

with

$$C_e = \ln \left(\frac{e}{c} \frac{kT}{2\pi h \rho_0^2 |\rho_{GJ}|} \right) \simeq 31 + \ln(P_0 T_6) \sim 30, \quad (30)$$

where $T_6 = T/(10^6 \text{ K})$ and P_0 is the spin period in units of 1 s. For a typical set of pulsar parameters (e.g., $P_0 = 1$ and $T_6 = 0.5$) $C_e \sim 30$, but C_e can range from 23 for millisecond pulsars to 35 for some magnetars. Note that the requirement $\phi \gg kT$ is automatically satisfied here when $|\rho_e|$ is less than $|\rho_{GJ}|$. The electron work function was calculated in ML06b and is depicted in Fig. 4.

4.1.2 Ion Emission

For neutron stars with $\mathbf{\Omega} \cdot \mathbf{B}_p < 0$, the Goldreich-Julian charge above the polar cap is positive, so we are interested in ion emission from the surface. Unlike the electrons, which form a relatively free-moving gas within the condensed matter, the ions

are bound to their lattice sites.¹ To escape from the surface, the ions must satisfy three conditions. First, they must be located on the surface of the lattice. Ions below the surface will encounter too much resistance in trying to move through another ion's cell. Second, they must have enough energy to escape as unbound ions. This binding energy that must be overcome will be labeled \mathcal{E}_B . Third, they must be thermally activated. The energy in the lattice is mostly transferred by conduction, so the ions must wait until they are bumped by atoms below to gain enough energy to escape.

Consider the emission of ions with charge $Z_n e$ from the neutron star surface (e.g., Fe^+ would have $Z_n = 1$). The rate of collisions between any two ions in the lattice is approximately equal to the lattice vibration frequency ν_i , which can be estimated from

$$\nu_i = \frac{1}{2\pi} (\Omega_p^2 + \omega_{ci}^2)^{1/2}, \quad (31)$$

where $\Omega_p = (4\pi Z^2 e^2 n_i / m_i)^{1/2}$ is the ion plasma (angular) frequency and $\omega_{ci} = ZeB / (m_i c)$ is the ion cyclotron frequency ($m_i = Am_p$). Not all collisions will lead to ejection of ions from the surface, since an energy barrier \mathcal{E}_B must be overcome. Thus each surface ion has an effective emission rate of order

$$\chi = \nu_i e^{-\mathcal{E}_B / kT}. \quad (32)$$

The energy barrier \mathcal{E}_B for ejecting ions of charge $Z_n e$ is equivalent to the energy required to release a neutral atom from the surface and ionize it, minus the energy gained by returning the electron to the surface (e.g., Tsong 1990). Thus

$$\mathcal{E}_B = Q_s + \sum_{i=1}^{Z_n} I_i - Z_n \phi, \quad (33)$$

where $Q_s > 0$ is the cohesive energy, $I_i > 0$ is the i th ionization energy of the atom (so that $\sum_{i=1}^{Z_n} I_i$ is the energy required to remove Z_n electrons from the atom), and $\phi > 0$ is the electron work function. The surface density of ions is $n_i r_i$, where r_i is the mean spacing between ions in the solid. Thus the emission flux of Z_n -ions is

$$\mathcal{F}_i = \nu_i n_i r_i e^{-\mathcal{E}_B / kT}. \quad (34)$$

The steady-state Z_n -ion number density supplied by the surface is then

$$\rho_i = \frac{Z_n e}{c} \mathcal{F}_i = \rho_{GJ} \exp(C_i - \mathcal{E}_B / kT), \quad (35)$$

with

$$\begin{aligned} C_i &= \ln \left(\frac{Z_n e \nu_i n_i r_i}{c \rho_{GJ}} \right) \\ &\simeq 34 + \ln \left\{ Z_n Z A^{-1/2} n_{28}^{3/2} (r_i / a_0) B_{12}^{-1} P_0 \sqrt{1 + 5.2 \times 10^{-3} A^{-1} B_{12}^2 n_{28}^{-1}} \right\} \sim 27-33, \end{aligned} \quad (36)$$

where $n_{28} = n_i / (10^{28} \text{ cm}^{-3})$. For a typical set of pulsar parameters (e.g., $B_{12} = 1$ and $P_0 = 1$) $C_i \sim 27$, but C_i can be as large as 33 for magnetars with $B_{12} = 1000$ and $P_0 = 8$.

All the quantities in \mathcal{E}_B were calculated in ML06b (see Figs. 2 and 3). We find that the emission of singly-ionized atoms ($Z_n = 1$) is most efficient, as \mathcal{E}_B is significantly lower for $Z_n = 1$ than for $Z_n > 1$ ($\sum_{i=1}^{Z_n} I_i$ grows much faster with Z_n than $Z_n \phi$ does).

4.1.3 Effect of Electric Field on Charge Emission

The discussion in Sections 4.1.1 and 4.1.2 includes only thermal emission of charged particles from the condensed surface. A strong electric field, of order $E_s \sim \Omega B R / c$, may be present. Since this electric field is much less than the characteristic field $\sim e / r_i^2$ inside the condensed matter (where r_i is the mean particle separation), this field cannot directly rip charges off the surface. Nevertheless, the electric field may enhance the thermal emission of charge particles. We now estimate the magnitude of this effect.

In the presence of a vacuum gap, the electric field E_s at the stellar surface points outward ($E_s > 0$) for stars with $\mathbf{\Omega} \cdot \mathbf{B}_p < 0$ and inward ($E_s < 0$) for stars with $\mathbf{\Omega} \cdot \mathbf{B}_p > 0$. A charge Q moved to some small height z above the surface gains a potential energy given by $U = -Q^2 / (4z) - Q E_s z$, where the first term is due to the interaction between the charge and the perfectly conducting metal surface, and the second term is due to the external field.² The potential reaches a maximum value

¹ The freezing condition is easily satisfied for condensed matter of heavy elements (see van Adelsberg et al. 2005).

² In the vacuum gap, the electric field is not exactly uniform, but since the maximum U is attained at a rather small height compared to the gap thickness, this nonuniformity is unimportant for our consideration here.

$$U_{\max} = -|Q|^{3/2}|E_s|^{1/2} \quad (37)$$

at the height $z = |Q/4E_s|^{1/2}$. Thus, compared to the $E_s = 0$ case, the energy barrier for particle emission is now reduced by the amount U_{\max} .

Combining this consideration with the results of Sections 4.1.1 and 4.1.2, we find that steady-state charge density due to electron surface emission (for $\boldsymbol{\Omega} \cdot \mathbf{B}_p > 0$ stars) is (cf. Jessner et al. 2001)

$$\rho_e = \rho_{GJ} \exp[C_e - (\phi - e^{3/2}|E_s|^{1/2})/kT], \quad (38)$$

and the steady-state charge density due to ion surface emission (for $\boldsymbol{\Omega} \cdot \mathbf{B}_p < 0$ stars) is

$$\rho_i = \rho_{GJ} \exp[C_i - (\mathcal{E}_B - (Z_n e)^{3/2}|E_s|^{1/2})/kT]. \quad (39)$$

For $E_s \sim \Omega BR/c$, we have $e^{3/2}|E_s|^{1/2} \sim 10$ eV. This is typically much smaller than either ϕ or \mathcal{E}_B .

4.2 Conditions for Gap Formation

No vacuum gap will form if the electrons or ions are able to fill the magnetosphere region above the polar cap with the required Goldreich-Julian density; i.e., the vacuum gap will cease to exist when $\rho_e = \rho_{GJ}$ or $\rho_i = \rho_{GJ}$. From Eqs. (39) and (38) we can see that no polar gap will form if

$$\phi - e^{3/2}|E_s|^{1/2} < C_e kT \sim 3T_6 \text{ keV} \quad (40)$$

for a negative polar magnetosphere ($\boldsymbol{\Omega} \cdot \mathbf{B}_p > 0$), and

$$\mathcal{E}_B - (Z_n e)^{3/2}|E_s|^{1/2} < C_i kT \sim 3T_6 \text{ keV} \quad (41)$$

for a positive polar magnetosphere ($\boldsymbol{\Omega} \cdot \mathbf{B}_p < 0$). [For the exact expressions for C_e and C_i see Eqs. (30) and (36).]

For neutron stars in general, the electron work function ϕ is much less than $C_e kT \sim 3T_6$ keV (see Fig. 4), so electrons can easily escape from the condensed surface. No gap forms for a negative polar magnetosphere under neutron star surface conditions. (This is contrary to the conclusions of Usov & Melrose 1996 and Gil et al. 2003.) The ion binding energy \mathcal{E}_B [given by Eq. (33)], on the other hand, can be larger than $C_i kT \sim 3T_6$ keV under certain neutron star surface conditions (see Figs. 1, 2, and 3). Ions can tightly bind to the condensed surface and a polar gap can form under these conditions. Figure 7 shows the critical temperature (determined by $\mathcal{E}_B = C_i kT$) below which a vacuum gap can form for the Fe, C, and He surfaces.

5 VACUUM GAP ACCELERATORS: PAIR CASCADES AND THE PULSAR DEATH LINE/BOUNDARY

Pair cascading in the magnetosphere of a pulsar is an essential ingredient for its radio emission (e.g., Melrose 2004). The pair cascade involves: (a) acceleration of primary particles by an electric field parallel to the magnetic field; (b) gamma ray emission by the accelerated particles moving along the magnetic field lines (either by curvature radiation or inverse Compton upscattering of surface photons); (c) photon decay into pairs as the angle between the photon and the field line becomes sufficiently large. To initiate the cascade an acceleration region is required; the characteristics of this particle accelerator determine whether pulsar emission can operate or not (the so-called ‘‘pulsar death line’’; e.g., Ruderman & Sutherland 1975; Arons 2000; Zhang et al. 2000; Hibschan & Arons 2001). Depending on the boundary condition at the neutron star surface, there are two types of polar gap accelerators: If charged particles are strongly bound to the neutron star surface by cohesive forces, a vacuum gap develops directly above the surface, with height h much less than the stellar radius (Ruderman & Sutherland 1975); if charged particles can be freely extracted from the surface, a more extended space-charge-limited-flow (SCLF) type accelerator develops due to field line curvatures (Arons & Scharlemann 1979) and the relativistic frame dragging effect (e.g., Muslimov & Tsygan 1992). Because the cohesive strength of matter at $B \sim 10^{12}$ G was thought to be negligible (based on the result of Neuhauser et al. 1987), most theoretical works in recent years have focused on the SCLF models (e.g., Arons 2000; Muslimov & Harding 2003, 2004).

Our results in Section 4 show that for sufficiently strong magnetic fields and/or low surface temperatures, a vacuum gap accelerator can form. Such a vacuum gap may be particularly relevant for the so-called high-B radio pulsars, which have inferred magnetic fields similar to those of magnetars (e.g., Kaspi & McLaughlin 2005; Burgay et al. 2006). In this section we discuss the conditions under which a vacuum gap will be an effective generator of pulsar emission. As discussed in Section 4, since electrons are weakly bound to the condensed stellar surface, such a vacuum gap is possible only for pulsars with $\boldsymbol{\Omega} \cdot \mathbf{B}_p < 0$ (as suggested in the original Ruderman-Sutherland model).

Our analysis is similar to the original Ruderman-Sutherland model, except that we extend our discussion of the cascade physics to the magnetar field regime, which introduces some corrections to previous works (e.g., Ruderman & Sutherland 1975; Usov & Melrose 1996). We also consider photon emission due to inverse Compton scattering, in addition to curvature radiation, in the cascade (cf. Zhang et al. 1997, 2000; Hibschan & Arons 2001).

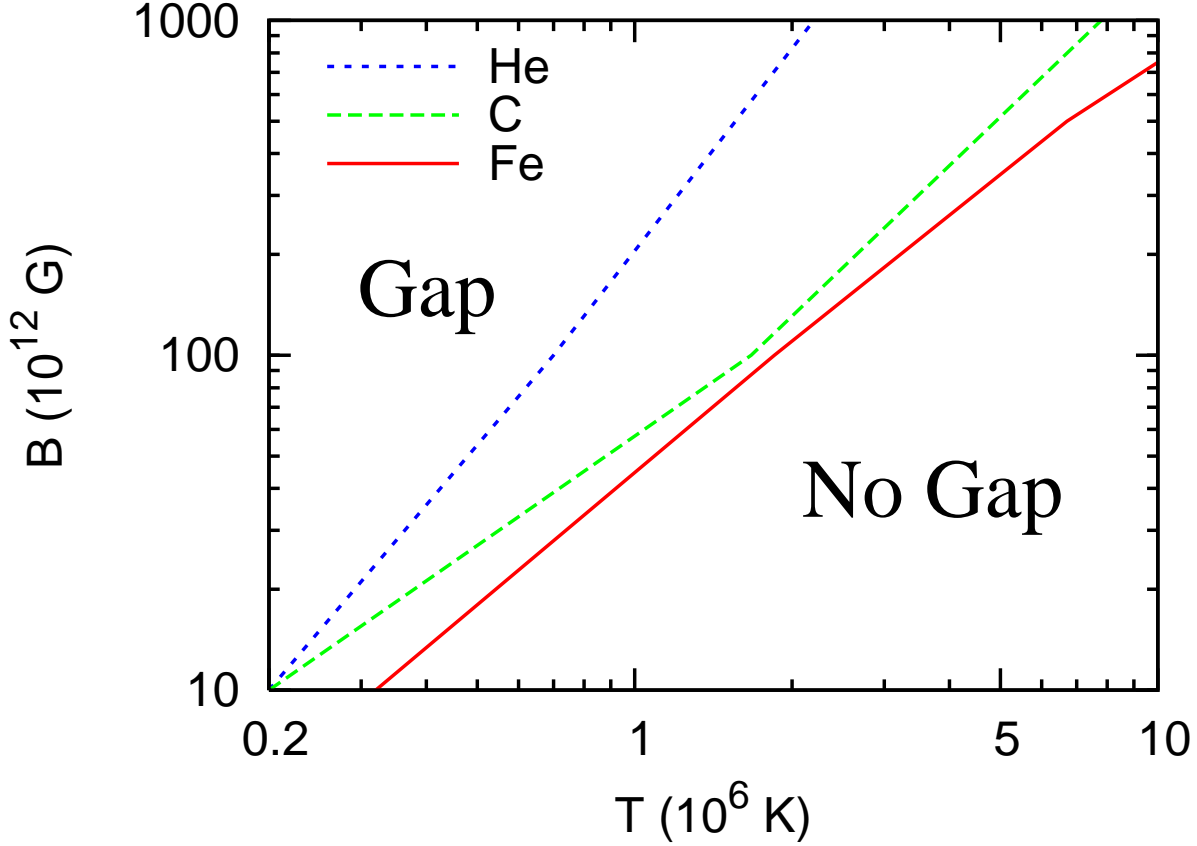


Figure 7. The condition for the formation of a vacuum gap above condensed helium, carbon, and iron neutron star surfaces, when the magnetosphere is positive over the poles ($\Omega \cdot \mathbf{B}_p < 0$).

5.1 Acceleration Potential

When the temperature drops below the critical value given in Section 4, the charge density above the polar cap decreases quickly below ρ_{GJ} , and a vacuum gap results. In the vacuum region just above the surface ($0 \leq z \ll R$), the parallel electric field satisfies the equation $dE_{\parallel}/dz \simeq -4\pi\rho_{GJ}$. The height of the gap h ($\ll R$) is determined by vacuum breakdown due to pair cascade, which shorts out the electric field above the gap (i.e., $E_{\parallel} = 0$ for $z \geq h$). Thus the electric field in the gap is

$$E_{\parallel} \simeq \frac{2\Omega B_p}{c}(h - z), \quad (42)$$

where $B_p = b_d B_p^d$ is the actual magnetic field at the pole, and differs from the dipole field B_p^d by a factor $b_d \geq 1$. The potential drop across the gap is then

$$\Delta\Phi = \frac{\Omega B_p}{c} h^2 = b_d \frac{\Omega B_p^d}{c} h^2. \quad (43)$$

With this potential drop, the electrons and positrons can be accelerated to a gamma factor

$$\gamma_m = \frac{e\Delta\Phi}{m_e c^2} = 5.43 \times 10^6 \beta_Q h_3^2 P_0^{-1} = 1.23 \times 10^5 b_d B_{12} h_3^2 P_0^{-1}, \quad (44)$$

where $\beta_Q = B_p/B_Q$ (with $B_Q = m_e^2 c^3 / e\hbar = 4.414 \times 10^{13}$ G the QED field), $B_{12} = B_p^d / (10^{12}$ G), $h_3 = h / (10^3$ cm) and P_0 is the spin period in units of 1 s. The voltage drop across the gap can be no larger than the voltage drop across the polar cap region $\Delta\Phi_{max} \simeq (\Omega B_p / 2c)(r_{p+})^2 = (\Omega B_p^d / 2c)(r_{p+}^d)^2$, where $r_{p+} = r_{p+}^d / b_d^{1/2}$ is the radius of the polar cap through which a net positive current flows:

$$r_{p+}^d = \left(\frac{2}{3}\right)^{3/4} R \left(\frac{\Omega R}{c}\right)^{1/2}. \quad (45)$$

Thus the gap height is limited from above by

$$h_{max} \simeq \frac{r_{p+}^d}{\sqrt{2b_d}} = 7.54 \times 10^3 b_d^{-1/2} P_0^{-1/2} \text{ cm}, \quad (46)$$

where we have adopted $R = 10$ km.

The above equations are for an aligned rotator. For an oblique rotator (where the magnetic dipole axis is inclined relative to the rotation axis), the voltage drop across the polar cap region is larger, of order $(\Omega B_p/2c)Rr_{p+}$. But as discussed in Appendix A, the acceleration potential across the vacuum gap is still limited from above by $\Delta\Phi_{max} \sim (\Omega B_p/2c)r_{p+}^2$.

5.2 Requirements for Gap Breakdown

There are two requirements for the breakdown of a vacuum gap. First, the photons must be able to create electron-positron pairs within the gap, i.e., the mean free path of photon pair-production is less than the gap height:

$$l_{\text{ph}} < h. \quad (47)$$

Second, the electrons and positrons must be accelerated over the gap potential and produce at least several photons within the gap. If on average only one photon is emitted with the required energy for each electron-positron pair, for instance, then the number of charged particles produced in the gap will grow very slowly and the gap will not break down completely. Therefore, we must have

$$N_{\text{ph}} > \lambda, \quad (48)$$

where N_{ph} is the number of photons emitted within the gap by each electron or positron, and λ is a number of order 1–10.

5.3 Pair Production

The threshold of pair production for a photon with energy ϵ is

$$\frac{\epsilon}{2m_e c^2} \sin \theta > 1, \quad (49)$$

where θ is the angle of intersection of the photon and the magnetic field. Suppose a photon is emitted at an angle θ_e . After the photon travels a distance z , the intersection angle will grow as z/\mathcal{R}_c , where \mathcal{R}_c is the local radius of curvature of the polar magnetic field line. Thus the typical intersection angle (for a photon crossing the entire gap) is

$$\sin \theta \simeq \theta \simeq \frac{h}{\mathcal{R}_c} + \theta_e. \quad (50)$$

For a pure dipole field, the curvature radius is of order $(Rc/\Omega)^{1/2} \simeq 10^8 P_0^{1/2}$ cm, but a more complex field topology at the polar cap could reduce \mathcal{R}_c to as small as the stellar radius.

In the weak-field regime, when the threshold condition is well-satisfied (so that the pairs are produced in highly excited Landau levels), the mean free path is given by (Erber 1966)

$$l_{\text{ph}} \simeq \frac{4.4a_0}{\beta_Q \sin \theta} \exp\left(\frac{4}{3\chi}\right), \quad \text{with } \chi = \frac{\epsilon}{2m_e c^2} \beta_Q \sin \theta, \quad (51)$$

where $a_0 = \hbar^2/(m_e c^2)$ is the Bohr radius. The condition $l_{\text{ph}} < h$ implies $\chi \gtrsim 1/15$ for typical parameters (Ruderman & Sutherland 1975). For stronger magnetic fields ($\beta_Q \gtrsim 0.1 - 0.2$), the pairs tend to be produced at lower Landau levels. Using the general expression for the pair production rate (e.g., Daugherty & Harding 1983), one can check that if the threshold condition Eq. (49) is satisfied, the pair-production optical depth across the gap would also be greater than unity [for $\beta_Q = 0.1$, the optical depth τ is unity when $\epsilon/(2m_e c^2) \sin \theta > 1.05$, and by $\beta_Q = 0.2$, $\tau = 1$ when $\epsilon/(2m_e c^2) \sin \theta > 1 + 10^{-7}$.] Thus for arbitrary field strengths, the condition $l_{\text{ph}} < h$ leads to the constraint:

$$\frac{\epsilon}{2m_e c^2} \beta_Q \left(\frac{h}{\mathcal{R}_c} + \theta_e \right) \gtrsim \frac{1}{15} (1 + 15\beta_Q). \quad (52)$$

5.4 Photon Emission Multiplicity and the Pulsar Death Line/Boundary

There several possible photon emission mechanisms operating in the vacuum breakdown, each leading to a different “death line”, or more precisely, “death boundary”. We consider them separately.

5.4.1 Curvature Radiation (CR)

The characteristic energy of a photon emitted through curvature radiation is $\epsilon \sim (3/2)\gamma^3 \hbar c/\mathcal{R}_c = 4.74 \times 10^9 \beta_Q^3 h_3^6 P_0^{-3} \mathcal{R}_6^{-1}$ eV, where $\mathcal{R}_6 = \mathcal{R}_c/(10^6 \text{ cm})$, and we have used $\gamma \sim \gamma_m$ [Eq. (44)]. The emission angle is $\theta_e \sim \gamma^{-1}$, which is typically much less than h/\mathcal{R}_c (this can be easily checked *a posteriori*). Equation (52) then reduces to

$$h > h_{\min, \text{ph}} = 546 P_0^{3/7} \mathcal{R}_6^{2/7} \left(\frac{15\beta_Q + 1}{\beta_Q^4} \right)^{1/7} \text{ cm.} \quad (53)$$

The rate of energy loss of an electron or positron emitting curvature radiation is $P_{\text{CR}} = 2e^2\gamma^4/(3c^3)(c^2/\mathcal{R}_c)^2$, thus the number of photons emitted through curvature radiation by a single electron or positron across the gap is

$$N_{\text{ph}} \simeq \frac{P_{\text{CR}}}{\epsilon} \frac{h}{c} \simeq \frac{4}{9} \frac{e^2}{\hbar c} \frac{\gamma h}{\mathcal{R}_c} = 17.6 \beta_Q h_3^3 P_0^{-1} \mathcal{R}_6^{-1}. \quad (54)$$

The condition $N_{\text{ph}} > \lambda$ [Eq. (48)] then gives

$$h \gtrsim h_{\min, \text{e}} = 384 \lambda^{1/3} \beta_Q^{-1/3} P_0^{1/3} \mathcal{R}_6^{1/3} \text{ cm.} \quad (55)$$

Thus the minimum gap height required for vacuum breakdown is $h \simeq \max(h_{\min, \text{ph}}, h_{\min, \text{e}})$. Combining Eqs. (46), (53), and (55), we have

$$\max(h_{\min, \text{ph}}, h_{\min, \text{e}}) < h_{\max}. \quad (56)$$

This gives a necessary condition for pulsar emission and defines the pulsar “death line”. For all relevant parameter regimes, $h_{\min, \text{ph}} > h_{\min, \text{e}}$, and Eq. (56) simply becomes $h_{\min, \text{ph}} < h_{\max}$. The critical pulsar spin period is then

$$P_{\text{crit}} = 1.64 b_d^{1/13} B_{12}^{8/13} \mathcal{R}_6^{-4/13} (1 + 15\beta_Q)^{-2/13} \text{ s,} \quad (57)$$

where the dipole polar field is $B_{12} = 2.0(P_0 \dot{P}_{15})^{1/2}$, with $\dot{P}_{15} = \dot{P}/(10^{-15} \text{ s s}^{-1})$. For $\beta_Q \lesssim 1/15$ this is the same as the result of Ruderman & Sutherland (1975).

In Fig. 8, we show the death lines determined from Eq. (56) for the cases of $\mathcal{R}_6 = 1$ and $\mathcal{R}_6 = 100 P_0^{1/2}$ (pure dipole field at the polar cap), with $b_d = 1$.

5.4.2 Resonant Inverse Compton Scattering (RICS)

Here the high-energy photons in the cascade are produced by Compton upscatterings of thermal photons from the neutron star surface. Resonant scattering in strong magnetic fields (e.g., Herold 1979) can be thought of as resonant absorption (where the electron makes a transition from the ground Landau level to the first excited level) followed by radiative decay. Resonance occurs when the photon energy in the electron rest frame satisfies $\epsilon' \simeq \epsilon_c = \hbar(eB/m_e c) = \beta_Q m_e c^2$. The resonant photon energy (in the “lab” frame) before scattering is $\epsilon_i = \epsilon_c / [\gamma(1 - \cos \theta_i)]$, where θ_i is the incident angle (the angle between the incident photon momentum and the electron velocity). After absorbing a photon, the electron Lorentz factor drops to $\gamma_e = \gamma / (1 + 2\beta_Q)^{1/2}$, and then radiatively decays isotropically in its rest frame. The characteristic photon energy after resonant scattering is therefore (e.g., Beloborodov & Thompson 2007)

$$\epsilon = \gamma \left(1 - \frac{1}{\sqrt{1 + 2\beta_Q}} \right) m_e c^2, \quad (58)$$

with typical emission angle $\theta_e \sim 1/\gamma_e$. The condition $l_{\text{ph}} < h$ [see Eq. (52)] becomes

$$\frac{\gamma}{2} \left(1 - \frac{1}{\sqrt{1 + 2\beta_Q}} \right) \beta_Q \left(\frac{h}{\mathcal{R}_c} + \frac{\sqrt{1 + 2\beta_Q}}{\gamma} \right) \gtrsim \beta_Q + \frac{1}{15}. \quad (59)$$

For $\beta_Q \gtrsim 4$ this condition is automatically satisfied, i.e., resonant ICS photons pair produce almost immediately upon being upscattered. For $\beta_Q < 4$, Eq. (59) puts a constraint on the gap height h . As we shall see below, most of the scatterings in the gap are done by electrons/positrons with $\gamma \sim \min(\gamma_c, \gamma_m)$, where $\gamma_c = \epsilon_c/kT$ (with T the surface blackbody temperature) and γ_m is the Lorentz factor of a fully-accelerated electron or positron [Eq. (44)]. For $\gamma = \gamma_m$, Eq. (59) yields

$$h \gtrsim h_{\min, \text{ph}}^{(1)} = 56.9 P_0^{1/3} \mathcal{R}_6^{1/3} f(\beta_Q)^{1/3} \text{ cm,} \quad (60)$$

where

$$f(\beta_Q) = \frac{\sqrt{1 + 2\beta_Q}}{\beta_Q} \left(\frac{2}{\sqrt{1 + 2\beta_Q} - 1} \frac{1 + 15\beta_Q}{15\beta_Q} - 1 \right). \quad (61)$$

For $\gamma = \gamma_c$ we have

$$h \gtrsim h_{\min, \text{ph}}^{(2)} = 169 \mathcal{R}_6 T_6 f(\beta_Q) \text{ cm.} \quad (62)$$

Combining Eqs. (60) and (62), we find that the condition $l_{\text{ph}} < h$ leads to

$$h \gtrsim h_{\min, \text{ph}} = \max(h_{\min, \text{ph}}^{(1)}, h_{\min, \text{ph}}^{(2)}). \quad (63)$$

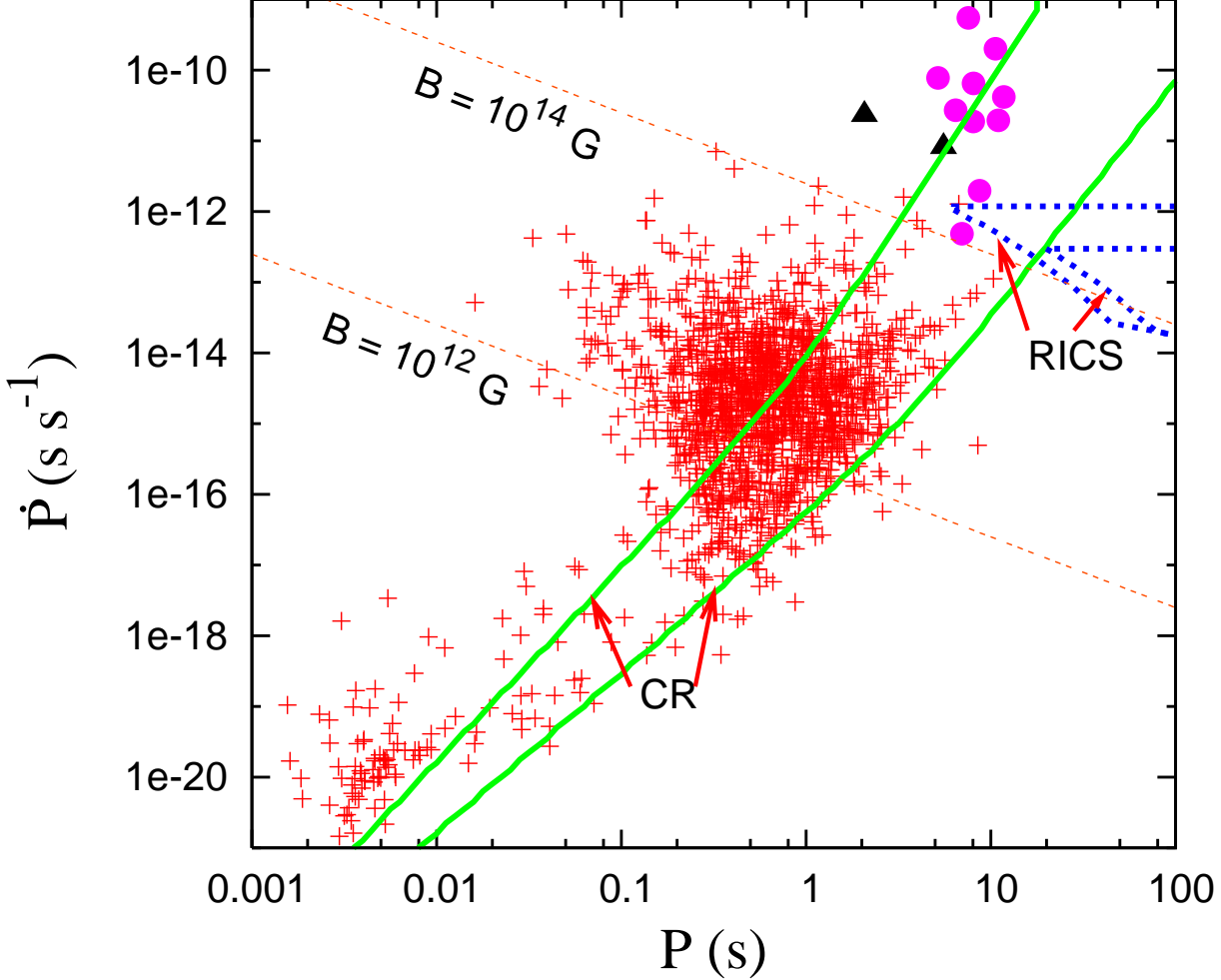


Figure 8. Pulsar death lines/boundaries for the CR and resonant ICS gap breakdown mechanisms. For curvature radiation, the lower line is for a magnetic field radius of curvature comparable to the stellar radius ($\mathcal{R}_c \simeq R$) and the upper line is for a radius curvature given by the dipole formula ($\mathcal{R}_6 = 100P_0^{1/2}$). For RICS, the large “box” is for $\lambda = 1$ and the small box is for $\lambda = 2$; both boxes are for a surface temperature of 5×10^6 K. The unspecified neutron star parameters are taken to be unity (i.e., we set $b_d = 1$ and for RICS $\mathcal{R}_6 = 1$). The CR mechanism operates (and the pulsar is alive) above and to the left of the lines, and the RICS mechanism operates within the boxes. Radio/X-ray pulsars (ATNF catalog, <http://www.atnf.csiro.au/research/pulsar/psrcat>) are labeled by crosses, while magnetars (McGill catalog, <http://www.physics.mcgill.ca/~pulsar/magnetar/main.html>) are labeled by solid circles and the two radio magnetars are labeled by solid triangles.

The resonant cross section for inverse Compton scattering, in the rest frame of the electron before scattering, is

$$\sigma'_{\text{res}} \simeq 2\pi^2 \frac{e^2 \hbar}{m_e c} \delta(\epsilon' - \epsilon_c), \quad (64)$$

where $\epsilon' \sim \gamma \epsilon_i$. This cross section is appropriate even for $B_p > B_Q$, since the resonant condition $\epsilon' = \epsilon_c$ holds regardless of field strength (cf. Gonthier et al. 2000). The ambient spectral photon number density near the polar cap is

$$\frac{dn_{\text{ph}}}{d\epsilon_i} = \frac{\epsilon_i^2 / (\pi^2 \hbar^3 c^3)}{e^{\epsilon_i/kT} - 1}. \quad (65)$$

For concreteness, consider a positron produced at $z = 0$ with initial Lorentz factor $\gamma = 1$ and accelerated to $\gamma = \gamma_m$ after crossing the full gap.³ Neglecting the radiation reaction (see later), we have $\gamma - 1 = 2(\gamma_m - 1)(z/h - z^2/2h^2)$. The number of

³ We can also consider the general situation where a positron (electron) is created at some location within the gap with initial Lorentz factor much less than γ_m , travels upwards (downwards) across the gap and get accelerated to a final Lorentz factor of order γ_m . This would give similar result for N_{ph} .

photons upscattered through resonant ICS by the positron is given by (see Appendix B)

$$\begin{aligned}
 N_{\text{ph}} &\simeq \int_0^h dz \int_0^\infty d\epsilon_i \frac{dn_{\text{ph}}}{d\epsilon_i} \sigma'_{\text{res}} \\
 &\simeq \frac{\beta_Q^2}{(\gamma_m - 1) a_0} \frac{h}{a_0} \int_1^{\gamma_m} \frac{d\gamma}{\gamma^3 (e^{\epsilon_c/kT\gamma} - 1)} \left(1 - \frac{\gamma - 1}{\gamma_m - 1}\right)^{-1/2} \\
 &\simeq \frac{1}{\gamma_m} \left(\frac{kT}{m_e c^2}\right)^2 \frac{h}{a_0} \int_{x_m}^{\epsilon_c/(kT)} \frac{x dx}{(e^x - 1)(1 - x_m/x)^{1/2}}
 \end{aligned} \tag{66}$$

where we have used $\gamma_m \gg 1$ and

$$x_m = \frac{\epsilon_c}{\gamma_m kT} = \frac{\gamma_c}{\gamma_m} = 1.09 \times 10^{-3} h_3^{-2} P_0 T_6^{-1}. \tag{67}$$

Note that the second equality of Eq. (66) gives

$$\frac{dN_{\text{ph}}}{d \ln \gamma} \simeq \beta_Q^2 \frac{h}{\gamma_m a_0} \gamma^{-2} (e^{\gamma_c/\gamma} - 1)^{-1} (1 - \gamma/\gamma_m)^{-1/2}. \tag{68}$$

From this equation we see that for $\gamma_c = \epsilon_c/kT \lesssim \gamma_m$, $dN_{\text{ph}}/d \ln \gamma$ peaks at $\gamma \sim \gamma_c$, with $(dN_{\text{ph}}/d \ln \gamma)_{\gamma=\gamma_c} \sim N_{\text{ph}}$, while for $\gamma_c < \gamma \lesssim \gamma_m$, $dN_{\text{ph}}/d \ln \gamma$ is of order $(\gamma_c/\gamma)N_{\text{ph}}$; for $\gamma_c \gtrsim \gamma_m$, $dN_{\text{ph}}/d \ln \gamma \sim (\gamma/\gamma_m)N_{\text{ph}}$ peaks at $\gamma \sim \gamma_m$. Therefore, most of the scatterings in the gap are done by electrons/positrons with $\gamma \sim \min(\gamma_c, \gamma_m)$. Since we are interested in the regime $\epsilon_c/kT \gg 1$, the integral in the last equality of Eq. (66) depends only on x_m , and for our purpose it can be approximated as $(\pi^2/6)x_m(e^{x_m} - 1)^{-1}$. This approximation reproduces the exact integral in the $x_m \rightarrow 0$ limit. Thus we have

$$N_{\text{ph, res}} \simeq 4.89 \times 10^{-2} \beta_Q^{-1} T_6^{5/2} P_0^{1/2} F(x_m), \quad \text{with} \quad F(x_m) = \frac{x_m^{3/2}}{e^{x_m} - 1}. \tag{69}$$

The function $F(x_m)$ peaks at $x_m = 0.874$ with $F_{\text{max}} = 0.585$. Thus the condition $N_{\text{ph}} > \lambda$ necessarily requires $2.86 \times 10^{-2} \beta_Q^{-1} T_6^{5/2} P_0^{1/2} \gtrsim \lambda$, or

$$\beta_Q \lesssim \beta_{Q, \text{crit}} = 2.86 \times 10^{-2} \lambda^{-1} T_6^{5/2} P_0^{1/2}. \tag{70}$$

For a given $\beta_Q < \beta_{Q, \text{crit}}$, the condition $N_{\text{ph}} > \lambda$ is equivalent to $F(x) > 0.588 \beta_Q / \beta_{Q, \text{crit}}$, which limits x_m to the range $x_a < x_m < x_b$, where $x_{a,b}$ are determining by solving $F(x_m) = 0.588 \beta_Q / \beta_{Q, \text{crit}}$. This condition then translates to the constraint on h :

$$h_{\text{min, e}} < h < h_{\text{max, e}}, \tag{71}$$

where

$$h_{\text{min, e}} = 33 x_b^{-1/2} P_0^{1/2} T_6^{-1/2} \text{ cm}, \quad h_{\text{max, e}} = 33 x_a^{-1/2} P_0^{1/2} T_6^{-1/2} \text{ cm}. \tag{72}$$

In summary, vacuum breakdown involving RICS requires

$$\beta_Q < \beta_{Q, \text{crit}} \quad \text{and} \quad \max(h_{\text{min, ph}}, h_{\text{min, e}}) < \min(h_{\text{max}}, h_{\text{max, e}}), \tag{73}$$

where $\beta_{Q, \text{crit}}$, h_{max} , $h_{\text{min, ph}}$, $h_{\text{min, e}}$, $h_{\text{max, e}}$ are given by Eqs. (70), (46), (63) (note that $h_{\text{min, ph}} = 0$ for $\beta_Q \gtrsim 4$), and (72), respectively. In Fig. 8 we show the pulsar death boundary when RICS is most important for initiating a cascade in the vacuum gap, for the cases $\lambda = 1$ and $\lambda = 2$, with $b_d = 1$, $\mathcal{R}_6 = 1$, and $T_6 = 5$. Note that in Fig. 8 we have not plotted RICS death boundaries for the case of a dipole radius of curvature ($\mathcal{R}_6 = 100 P_0^{1/2}$) or a surface temperature $T_6 \lesssim 1$; there are no regions of the P - \dot{P} diagram where vacuum gap pair cascades are possible under these conditions.

The pulsar death boundary depicted in Fig. 8 can be understood as follows: (i) a) The condition $h_{\text{min, ph}}^{(1)} < h_{\text{max}}$ gives

$$\text{(Ia)} \quad P \lesssim 352 b_d^{-3/5} \mathcal{R}_6^{-2/5} f(\beta_Q)^{-2/5} \text{ s}, \tag{74}$$

where $f(\beta_Q)$ is given by Eq. (61). This is shown as the long-dashed line labeled (Ia) in Fig. 9. b) The condition $h_{\text{min, ph}}^{(2)} < h_{\text{max}}$ gives

$$\text{(Ib)} \quad P \lesssim 1.99 \times 10^3 b_d^{-1} \mathcal{R}_6^{-2} T_6^{-2} f(\beta_Q)^{-2} \text{ s}. \tag{75}$$

This is shown as the short-dashed line labeled (Ib) in Fig. 9. This set of conditions, (Ia) and (Ib), is the usual requirement that photons emitted by an accelerated electron or positron in the gap must be able initiate pair production. (ii) a) For $\beta_Q \ll \beta_{Q, \text{crit}}$, we have $x_a \simeq 0.342 (\beta_Q / \beta_{Q, \text{crit}})^2$, and the condition $h_{\text{min, ph}}^{(1)} < h_{\text{max, e}}$ then yields

$$\text{(IIa)} \quad P \gtrsim 210 \lambda^{3/2} \mathcal{R}_6^{1/2} T_6^{-3} \beta_Q^{3/2} f(\beta_Q)^{1/2} \text{ s}. \tag{76}$$

This is shown as the dotted line labeled (IIa) in Fig. 9. b) The condition $h_{\text{min, ph}}^{(2)} < h_{\text{max, e}}$ yields

$$(IIb) \quad P \gtrsim 105 \lambda \mathcal{R}_6 T_6^{-1} f(\beta_Q) \text{ s.} \quad (77)$$

This is shown as the dot-long-dashed line labeled (IIb) in Fig. 9. This set of conditions, (IIa) and (IIb), together with $\beta_Q \lesssim \beta_{Q,\text{crit}}$, come from the requirement for efficient photon emission by RICS in the gap. (iii) The condition $h_{\text{min},e} < h_{\text{max}}$ gives

$$(III) \quad P \lesssim 228 b_d^{-1/2} T_6^{1/2} x_b^{1/2} \text{ s,} \quad \text{with } x_b \sim 0.874 + \ln \frac{\beta_{Q,\text{crit}}}{\beta_Q}. \quad (78)$$

This condition is shown as the dot-short-dashed line labeled (III) in Fig. 9. (iv) The condition $\beta_Q > \beta_{Q,\text{crit}}$ gives Eq. (70) and is shown as the light solid line labeled (IV) in Fig. 9.

Previous studies of the the pulsar conditions for vacuum gaps where RICS is the dominant photon emission mechanism have found that the RICS mechanism can lead to gap breakdown for a wide range of neutron star parameters (see, e.g., Zhang et al. 2000). This is contrary to our results, which show (see Figs. 8 and 9) that RICS is not a good mechanism for gap breakdown, except under very specific conditions (e.g., high surface temperatures and long rotation periods). The discrepancy arises because previous works did not calculate/estimate N_{ph} (the number of high energy photons produced as a positron/electron crosses the gap) correctly. For example, it was implicitly assumed that photon production continues across the entire gap at the same rate as it does when $\gamma \simeq \gamma_c$ (i.e., at the point of maximum RICS power loss) (Zhang et al. 2000). This assumption is invalid for $\gamma > \gamma_c$, as is discussed above: $dN_{\text{ph}}/d\ln \gamma$ grows with increasing gamma factor until $\gamma \sim \gamma_c$, and then it decreases [see Eq. (68)]; therefore, $dN_{\text{ph}}/d\gamma$ (which is directly related to the photon production rate \dot{N}_{ph}) drops faster than γ^{-1} above $\gamma \sim \gamma_c$.

Note that the accelerating positron/electron is not radiation-reaction limited at $\gamma \simeq \gamma_c$, since the power loss due to RICS is significantly smaller than the power gain due to traversal across the potential drop. The power loss due to RICS is given by

$$P_{\text{loss}} = c \int_0^\infty d\epsilon_i \frac{dn_{\text{ph}}}{d\epsilon_i} \sigma'_{res}(\epsilon - \epsilon_i) \quad (79)$$

$$\simeq \frac{2\beta_Q^2 c}{a_0} \left(1 - \frac{1}{\sqrt{1+2\beta_Q}} \right) \frac{m_e c^2}{\gamma^2 (e^{\epsilon_c/kT\gamma} - 1)}. \quad (80)$$

At the point of maximum RICS power loss (when $\gamma = \gamma_c = \epsilon_c/kT$)

$$P_{\text{loss}}(\gamma = \gamma_c) \simeq \frac{2c}{a_0} \left(1 - \frac{1}{\sqrt{1+2\beta_Q}} \right) \left(\frac{kT}{mc^2} \right)^2 (e-1)^{-1} m_e c^2 \quad (81)$$

$$\simeq 1.9 \times 10^{11} \left(1 - \frac{1}{\sqrt{1+2\beta_Q}} \right) T_6^2 m_e c^2 \text{ s}^{-1} \quad (82)$$

(cf. Dermer (1990)). The power gain due to acceleration across the gap is given by

$$P_{\text{gain}} = e\mathcal{E}_{\parallel} c = \frac{2\Omega\beta_Q}{\alpha a_0} (h-z) m_e c^2. \quad (83)$$

Thus

$$\frac{P_{\text{gain}}}{P_{\text{loss}}}\Big|_{\gamma=\gamma_c} \simeq 170 \left(\frac{h-z}{100 \text{ cm}} \right) P_0^{-1} T_6^{-2} \beta_Q \left(1 - \frac{1}{\sqrt{1+2\beta_Q}} \right)^{-1}. \quad (84)$$

For most pulsar parameters, $P_{\text{gain}} \gg P_{\text{loss}}$ [e.g., in order for γ to reach γ_c the gap height must be at least $h = 33P_0^{1/2}T_6^{-1/2}$ cm; see Eq. (67) with $x_m = 1$]. Therefore, there is no reason why γ should remain near γ_c , the point of maximum RICS photon emission, as was assumed in some earlier papers.

5.4.3 Nonresonant Inverse Compton Scattering (NRICS)

The characteristic energy of a photon Compton-upscattered by an electron or positron of Lorenz factor γ is $\epsilon \sim \gamma\epsilon'/(1+x)$, where $x = \epsilon'/mc^2$, $\epsilon' \sim \gamma\epsilon_i$, and ϵ_i is the initial seed photon energy; the pitch angle of the scattered photon is of order $\theta_e \sim (1+x)/\gamma$. In the vacuum gap, most the scatterings are by electrons/positrons with $\gamma \sim \gamma_m$ on seed photons with initial energy $\epsilon_i \sim 2.82kT$ (see below). Substituting

$$\epsilon \sim \frac{\gamma_m \epsilon'_m}{1+x_m}, \quad \text{with } x_m = \frac{\epsilon'_m}{mc^2} = \frac{2.82kT\gamma_m}{mc^2} \quad (85)$$

into Eq. (52) (which results from the requirement $l_{\text{ph}} < h$), we find

$$\frac{\gamma_m}{2} \left(\frac{x_m}{1+x_m} \right) \beta_Q \left(\frac{h}{\mathcal{R}_c} + \frac{1+x_m}{\gamma_m} \right) > \beta_Q + \frac{1}{15}. \quad (86)$$

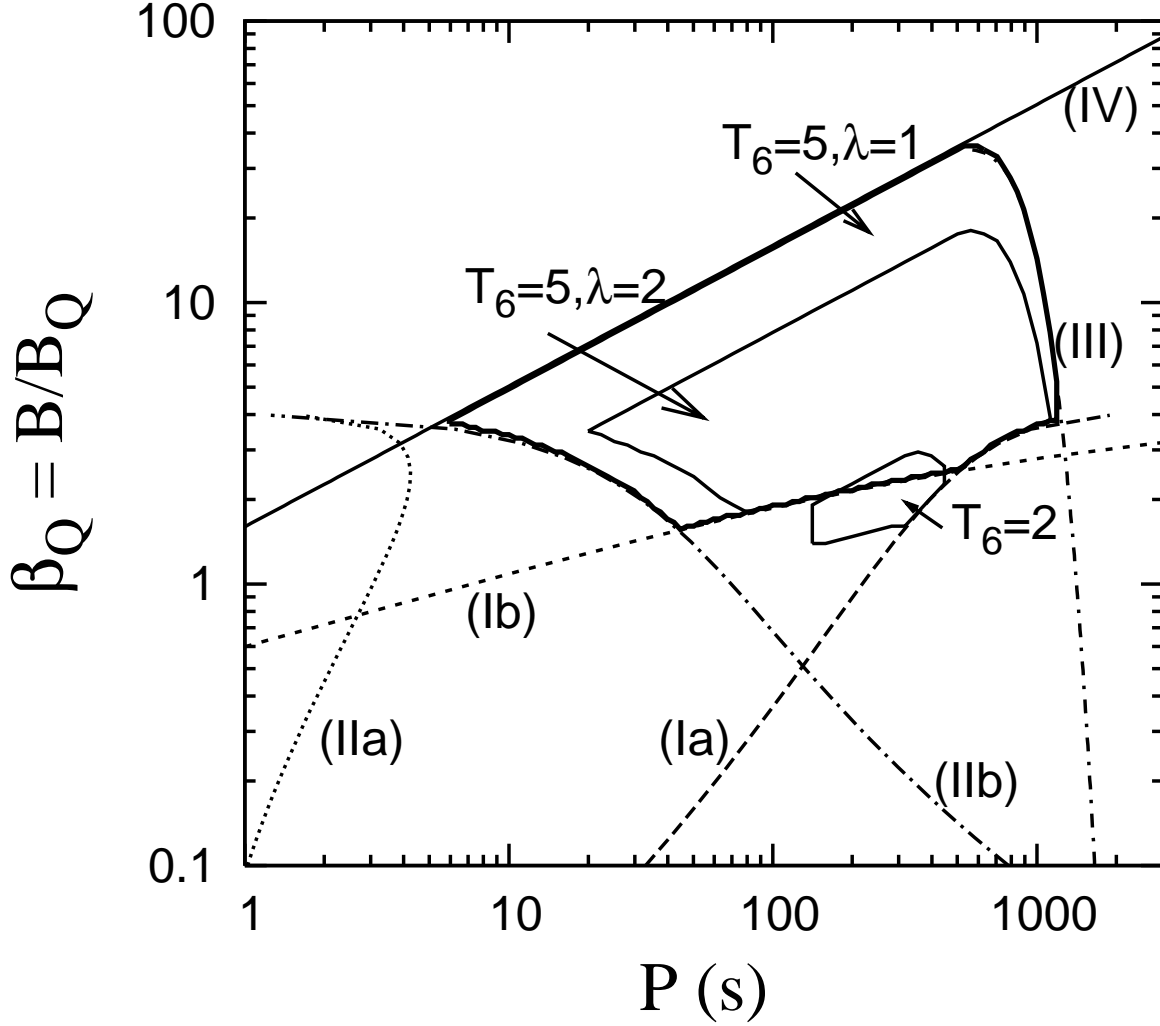


Figure 9. The pulsar death boundaries when the resonant ICS mechanism is most important for initiating a cascade, plotted as a function of the dimensionless magnetic field strength $\beta_Q = B/B_Q$ and the period P . The boundaries are shown for surface temperature $T = 5 \times 10^6$ K and parameter $\lambda = 1$ (the largest, bold, enclosed region), $T = 5 \times 10^6$ K and $\lambda = 2$ (the mid-sized enclosed region) and $T = 2 \times 10^6$ K and $\lambda = 1$ (the smallest enclosed region). The critical lines defining the edges of the region for $T_6 = 5, \lambda = 1$ are also shown. Each critical line (I)–(IV) is determined by one of Eqs. (74)–(78) and (70), as discussed in Section 5.4.2.

Using Eq. (44), this becomes

$$0.0415\beta_Q^{-1/2}P_0^{1/2}T_6^{-3/2}\mathcal{R}_6^{-1}\frac{x_m^{5/2}}{1+x_m} + x_m > 2\left(1 + \frac{1}{15\beta_Q}\right). \quad (87)$$

The gap height is related to x_m by

$$h = 19.7x_m^{1/2}\beta_Q^{-1/2}P_0^{1/2}T_6^{-1/2} \text{ cm}. \quad (88)$$

The solution to Eq. (87) yields $x_m > x_{\min}$, and thus the constraint on the gap height from $l_{\text{ph}} < h$ is

$$h \gtrsim h_{\min, \text{ph}} = 19.7x_{\min}^{1/2}\beta_Q^{-1/2}P_0^{1/2}T_6^{-1/2} \text{ cm}. \quad (89)$$

The nonresonant part of the ICS cross section, in the rest frame of the electron before scattering, is approximately given by

$$\sigma'(\epsilon') \simeq \sigma_T \left(\frac{\epsilon'}{\epsilon' + \epsilon_c}\right)^2 f_{\text{KN}}(x) = \sigma_T \left(\frac{x}{x + \beta_Q}\right)^2 f_{\text{KN}}(x), \quad (90)$$

where σ_T is the Thomson cross-section, $x = \epsilon'/(mc^2)$, and

$$f_{\text{KN}}(x) = \frac{3}{4} \left[\frac{1+x}{x^3} \left\{ \frac{2x(1+x)}{1+2x} - \ln(1+2x) \right\} + \frac{1}{2x} \ln(1+2x) - \frac{1+3x}{(1+2x)^2} \right] \quad (91)$$

is the Klein-Nishina suppression factor [$f_{\text{KN}} \simeq 1 - 2x$ for $x \ll 1$ and $f_{\text{KN}} \simeq (3/8x)(\ln 2x + 1/2)$ for $x \gg 1$]. This agrees well with the calculated NR cross sections in strong magnetic fields (e.g., Gonthier et al. 2000).

The number of scatterings per unit length by an electron or positron is

$$\frac{dN_{\text{ph}}}{dz} \simeq \int_0^\infty d\epsilon_i \frac{dn_{\text{ph}}}{d\epsilon_i} \sigma'(\gamma\epsilon_i) \sim 0.24 \left(\frac{kT}{\hbar c}\right)^3 \sigma'(2.82kT\gamma), \quad (92)$$

where in the second equality we have used the fact that $dn_{\text{ph}}/d\ln \epsilon_i$ peaks at $\epsilon_i = 2.82kT$, while $\sigma'(\epsilon')$ varies more slowly with ϵ' . Similar to Section 5.4.2, consider a positron produced at $z = 0$ with initial Lorentz factor $\gamma = 1$ and accelerated to $\gamma = \gamma_m$ after crossing the full gap. The number of scatterings produced by the positron is given by

$$N_{\text{ph}} \simeq \frac{h}{2\gamma_m} \int_1^{\gamma_m} \frac{d\gamma}{\sqrt{1 - \gamma/\gamma_m}} \frac{dN_{\text{ph}}}{dz}. \quad (93)$$

Clearly, most of the scatterings are by positrons/electrons with $\gamma \sim \gamma_m$, producing photons with energy $2.82kT\gamma_m^2/(1 + x_m)$ [see Eq. (85)]. The number of photons scattered by $\gamma = (0.7-1)\gamma_m$ electrons/positrons is

$$\begin{aligned} N_{\text{ph}} &\sim \frac{h}{2} \left(\frac{dN_{\text{ph}}}{dz}\right)_{\gamma=\gamma_m} \simeq 0.12 h \left(\frac{kT}{\hbar c}\right)^3 \sigma_T \left(\frac{x_m}{x_m + \beta_Q}\right)^2 f_{\text{KN}}(x_m) \\ &\simeq 1.3 \times 10^{-4} \beta_Q^{-1/2} T_6^{5/2} P_0^{1/2} F(x_m, \beta_Q), \end{aligned} \quad (94)$$

where

$$F(x_m, \beta_Q) = \frac{x_m^{5/2}}{(x_m + \beta_Q)^2} f_{\text{KN}}(x_m). \quad (95)$$

Now consider the vacuum breakdown condition $N_{\text{ph}} > \lambda$. For a given β_Q , the function $F(x_m, \beta_Q)$ has a maximum $F_{\text{max}}(\beta_Q)$ (this maximum is approximately achieved at $x_m \sim 2.24 + 3\beta_Q$). Then $N_{\text{ph}} > \lambda$ requires

$$P \gtrsim P_{\text{crit}}(\beta_Q) = 5.7 \times 10^7 \lambda^2 T_6^{-5} \beta_Q F_{\text{max}}(\beta_Q)^{-2} \text{ s}. \quad (96)$$

When this is satisfied, we additionally require

$$\frac{F(x_m, \beta_Q)}{F_{\text{max}}(\beta_Q)} > \left[\frac{P}{P_{\text{crit}}(\beta_Q)} \right]^{-1/2}, \quad (97)$$

which yields the solution $x_a < x_m < x_b$. In terms of the gap height, we have

$$h_{\text{min,e}} < h < h_{\text{max,e}}, \quad (98)$$

where

$$h_{\text{min,e}} = 19.7 x_a^{1/2} \beta_Q^{-1/2} P_0^{1/2} T_6^{-1/2} \text{ cm}, \quad h_{\text{max,e}} = 19.7 x_b^{1/2} \beta_Q^{-1/2} P_0^{1/2} T_6^{-1/2} \text{ cm}. \quad (99)$$

When the neutron star surface temperature $T_6 \leq 5$ there are no values of β_Q or P for which NRICS can initiate a cascade in the vacuum gap. (Only when $T_6 \gtrsim 9$ are there any β_Q, P values which permit an NRICS-initiated cascade, and even at these high temperatures the allowed range of β_Q and P values is very small and atypical of neutron stars.) Therefore, no pulsar death boundaries appear for the NRICS process in Fig. 8.

6 DISCUSSION

It is well known that a strong magnetic field increases the binding energy of individual atom and that of the zero-pressure condensed matter. Very approximately, for $B \gg B_0$ [see Eq. (1)], the former increases as $(\ln B)^2$ while the latter scales as $B^{0.4}$. Therefore one expects that the outermost layer of a neutron star may be in the condensed state when the magnetic field B is sufficiently strong and/or the surface temperature T is sufficiently low. Exactly under what conditions this occurs is an important question that entails quantitative calculations. In this paper, using our recent results on the cohesive properties of magnetized condensed matter (Medin & Lai 2006a,b), we have established quantitatively the parameter regime (in B and T space) for which surface condensation occurs. Our calculations showed that there are a range of neutron star magnetic field strengths and surface temperatures where the condensed surface will have an important effect on radiation from these stars. For example, if the surface composition is Fe, then strong-field neutron stars ($B \gtrsim 10^{13}$ G) with moderate ($T \lesssim 10^6$ K) surface temperatures should have atmospheres/vapors that are effectively transparent to thermal radiation, so that the emission becomes that from a bare condensed surface. This may explain the nearly blackbody-like radiation spectrum observed from the nearby isolated neutron star RX J1856.5-3754 (e.g., Burwitz et al. 2003; van Adelsberg et al. 2005; Ho et al. 2007).

We have also examined the conditions for the formation of a vacuum acceleration gap above the polar cap region of

the neutron star. The inner acceleration gap model, first developed by Ruderman & Sutherland (1975), has provided a useful framework to understand numerous observations of radio pulsars. Most notably, the model naturally explains the phenomenon of drifting subpulses observed in many pulsars (e.g., Backer 1976; Deshpande & Rankin 1999; Weltevrede et al. 2006) in terms of the $\mathbf{E} \times \mathbf{B}$ circulation of plasma filaments produced by vacuum discharges. Partially screened gaps have also been studied (e.g., Cheng & Ruderman 1980; Gil et al. 2003, 2006). However, it has long been recognized that the original Ruderman & Sutherland model is problematic since the dipole magnetic field inferred from P, \dot{P} may not be strong enough to inhibit charge emission from the surface. Our calculations described in this paper quantify the condition for vacuum gap formation (see Fig. 7). While this condition (i.e., T is smaller than a critical value which depends on B and composition) may not be satisfied for most pulsars (unless one invokes surface magnetic fields much stronger than that inferred from P, \dot{P} ; see Gil et al. 2006 and references therein), it could well be satisfied for some neutron stars. In particular, the recently discovered high-B radio pulsars, having dipole surface magnetic fields in excess of 10^{14} G and temperature about 10^6 K (e.g., Kaspi & Gavriil 2004; Kaspi & McLaughlin 2005), may operate a vacuum gap accelerator. On the other hand, while magnetars have similar magnetic field strengths, their surface temperatures are about five times larger than those of high-B radio pulsars, and therefore may not have a vacuum gap. In this regard, it is interesting to note that most magnetars do not show radio emission (though this may be because the radio pulse is beamed away from us or the because their magnetosphere plasma “overwhelms” the radio pulses), and the two recently detected radio magnetars have rather different radio emission properties (e.g., the spectrum extends to high frequency and the radiation shows high degrees of linear polarization) compared to “normal” radio pulsars. We may therefore speculate that a key difference between magnetars and high-B radio pulsars is their difference in surface temperature. In any case, our gap formation condition (Fig. 7) suggests that the radio emission property of neutron stars may depend not only on the magnetic field and rotation rate, but also on the surface temperature.

We note that our calculation of the requirements for vacuum gap formation assumes idealized conditions. A real neutron star polar cap may be immersed in a strong radiation field and suffer bombardment from high energy particles (e.g., Arons 1981; Beloborodov & Thompson 2007). The effective cohesive energy of the surface may be somewhat smaller than what we used in our paper due to surface defects (Arons 2007, private communication). Whether the vacuum gap survives in realistic situations is unclear. It has been suggested that a partially screened gap is formed instead (Gil et al. 2003, 2006). With small modifications [e.g., the potential drop given by Eq. (43) is reduced], our discussion of pair cascades in the vacuum gap can be easily generalized to the case of a partially screened gap.

A major part of our paper is devoted to the pair cascade physics in the vacuum gap (Section 5). We find that pair cascade initiated by curvature radiation can account for most pulsars in the $P-\dot{P}$ diagram, but significant field line curvature near the stellar surface is needed. Although such field curvature is possible for some pulsars, it is unlikely to occur for all of them. For a pure dipole magnetic field, only about half of all pulsars can be explained by a curvature radiation-initiated cascade. Contrary to previous works (e.g., Zhang et al. 2000), we find that inverse Compton scatterings (resonant or not) are not efficient in producing vacuum breakdown via pair cascade.

The recent detection of the radio emission from two AXPs (Camilo et al. 2006, 2007) is of great interest. The emission appears to be triggered by X-ray outbursts of usually quiescent magnetars. This may be due to a rearrangement of the surface magnetic field, which made pair cascades possible. We note that the occurrence of pair cascades depends strongly on the field line geometry/curvature; our study of pair cascades in the context of vacuum gap accelerators (Section 5) serves as an illustration of this point.

ACKNOWLEDGMENTS

This work has been supported in part by NASA Grant NNX07AG81G, NSF grants AST 0307252 and 0707628, and by *Chandra* grant TM6-7004X (Smithsonian Astrophysical Observatory).

APPENDIX A: MAXIMUM POTENTIAL DROP FOR AN OBLIQUE ROTATOR

For an oblique rotator, with the magnetic inclination angle α much larger than the polar cap angular size r_p/R , the voltage drop across the polar cap is of order $(\Omega B_p/c) R r_p \sin \alpha$, which is a factor of R/r_p larger than the aligned case. Here we show explicitly that the maximum potential drop across the height of the vacuum gap is still of order $(\Omega B_p/c) r_p^2$.

We will be working in the “lab” frame, where the star is rotating. For simplicity we approximate the vacuum gap to be a cylinder of radius r_p and height $h \ll R$; see Fig. A1. In reality the bases of the cylinder are not exactly circular for an oblique rotator, but this does not affect our conclusion. The gap is small compared to the stellar radius and we can treat it locally, using a Cartesian coordinate system: z along the gap height and x, y for the distance from the pole (with \hat{x} being principally along $\hat{\theta}$ and \hat{y} along $\hat{\phi}$; $\hat{\theta}$ points in the direction from the rotational pole to the magnetic pole). The magnetic field in the cylinder is approximately uniform, $\mathbf{B} = -B_p \hat{z}$.

The electric potential inside the cylindrical gap satisfies $\nabla^2 \Phi = 0$. The potential at the base and on the walls of the

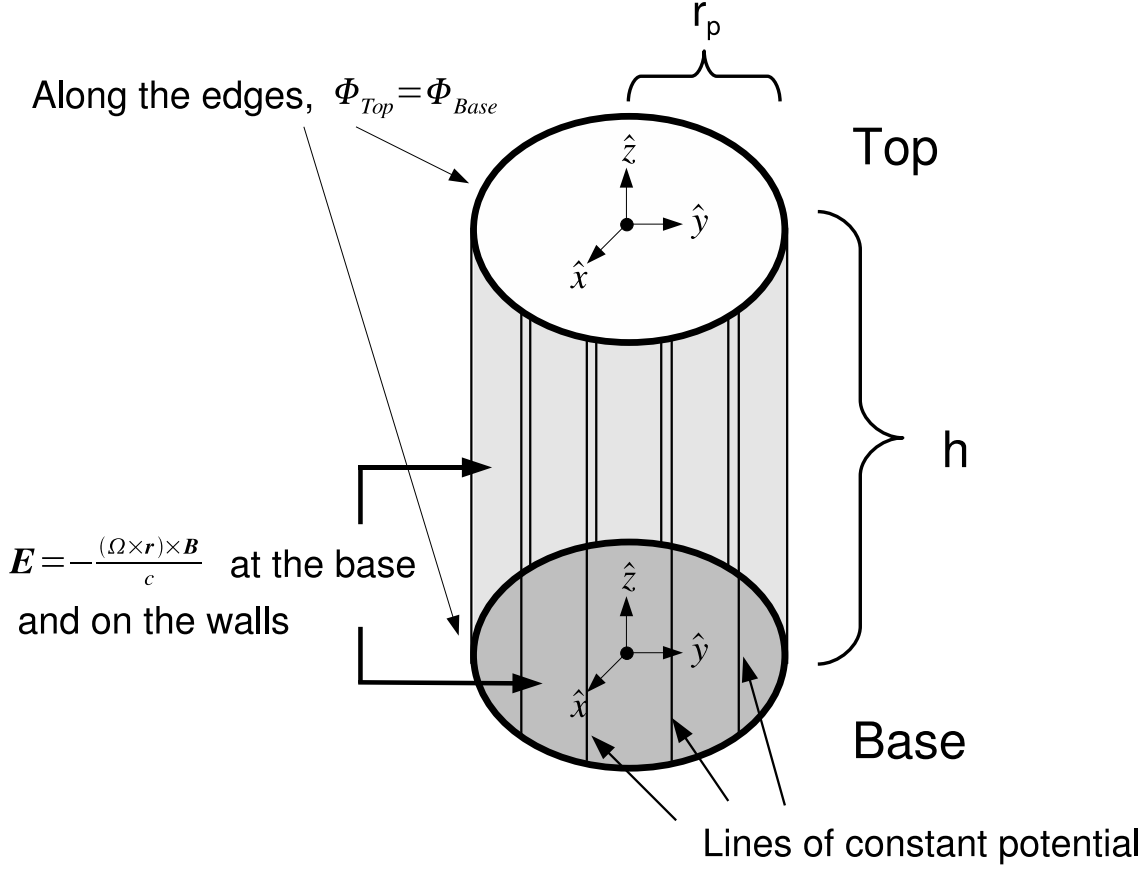


Figure A1. A schematic diagram showing the polar gap structure in the cylindrical approximation.

cylinder can be found from $\mathbf{E} = -c^{-1}[(\boldsymbol{\Omega} \times \mathbf{r}) \times \mathbf{B}]$. At the top of the cylinder, the potential satisfies $E_z = -\partial\Phi/\partial z = 0$. With these boundary conditions the potential within the cylinder is completely determined.

Without solving the complete potential problem, here we only consider the potential at the top of the cylinder in the limit of $h \gg r_p$ (but $h \ll R$); this corresponds to the maximum potential drop across the gap. In this limit, the electric field on the top satisfies not only $E_z = 0$ but also $dE_z/dz = 0$. Thus the Laplace equation below the top of the cylinder becomes

$$\frac{d^2\Phi}{dx^2} + \frac{d^2\Phi}{dy^2} = 0. \quad (\text{A1})$$

To lowest order in x/R and y/R the electric field below the base of the cylinder is given by

$$\mathbf{E} = -\frac{(\boldsymbol{\Omega} \times \mathbf{r}) \times \mathbf{B}}{c} \simeq \frac{\Omega B_p R}{c} \left[\left(\sin \alpha + \cos \alpha \frac{x}{R} \right) \hat{x} + \cos \alpha \frac{y}{R} \hat{y} \right]. \quad (\text{A2})$$

The potential at the base of the cylinder is therefore (using $\mathbf{E} = -\nabla\Phi$ and renormalizing such that the potential is zero at the pole)

$$\Phi_{\text{base}} = -\frac{\Omega B_p R^2}{c} \left[\sin \alpha \frac{x}{R} + \cos \alpha \left(\frac{x^2}{2R^2} + \frac{y^2}{2R^2} \right) \right]. \quad (\text{A3})$$

Since $E_z = 0$ on the cylindrical wall, the potential on the wall is also given by Eq. (A3). The potential at the top of the cylinder must solve Eq. (A1) and match the potential on the wall along the upper edge. For a circular polar cap boundary, given by $x^2 + y^2 = r_p^2$, the potential at the top is then

$$\Phi_{\text{top}} = -\frac{\Omega B_p R^2}{c} \left[\sin \alpha \frac{x}{R} + \cos \alpha \frac{r_p^2}{2R^2} \right]. \quad (\text{A4})$$

From Eqs. (A3) and (A4), we find that at the magnetic pole, $|\Phi_{\text{top}} - \Phi_{\text{base}}| \simeq (\Omega B_p r_p^2 / 2c) \cos \alpha$, which is the value of the aligned case multiplied by $\cos \alpha$. Figure A2 compares the potential at the base and top of the cylindrical gap along the x

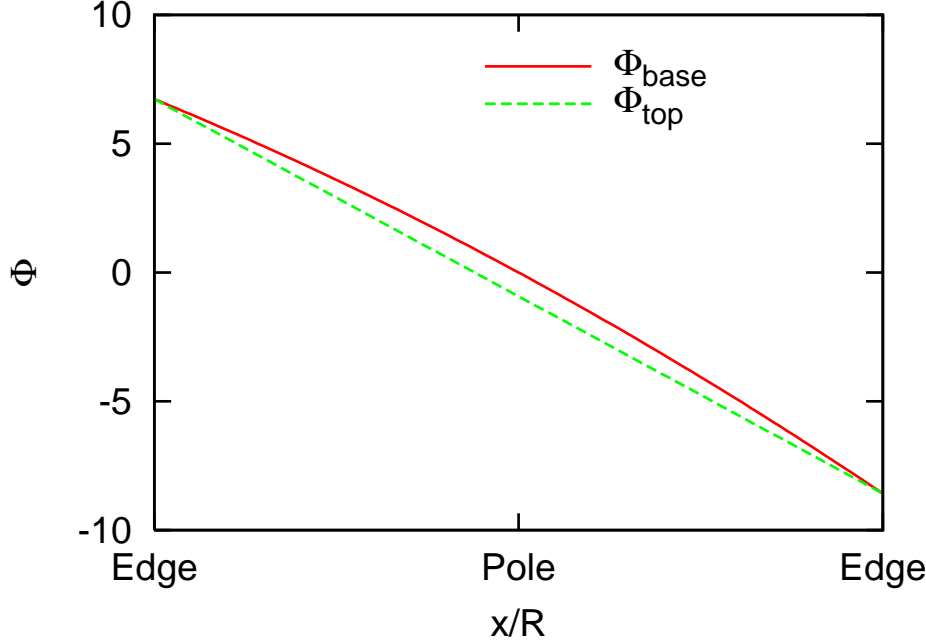


Figure A2. Potential along the \hat{x} ($\sim \hat{\theta}$) direction, through the magnetic pole, both at the stellar surface and at the top of the vacuum gap, for an oblique rotator. The magnetic inclination angle is chosen to be $\alpha = \pi/8$. The potential is measured in units of $\Omega B_p r_p^2/2c$, the value of the maximum potential drop for an aligned rotator case.

axis. We see that although there is a large potential drop across the polar cap, the potential difference between the top and the base is smaller.

Alternatively, we may examine the problem in the rotating frame, in which the potential inside the vacuum gap satisfies the equation $\nabla^2 \Phi = 4\pi \rho_{\text{GJ}}$, where ρ_{GJ} is the Goldreich-Julian charge density. The potential at the base and on the wall of the cylinder is $\Phi = 0$ (since the electric field is zero there). At the top of the cylinder, we have $\partial \Phi / \partial z = 0$. These boundary conditions completely determine the potential inside the cylinder. For $h \ll r_p$, we expect the potential drop along the z -axis, $\Delta \Phi$, to grow as h^2 . But when h becomes larger than r_p , the potential drop $\Delta \Phi$ will saturate to $(\Omega B_p r_p^2/2c) \cos \alpha$, similar to the aligned case.

APPENDIX B: SCATTERING RATE CALCULATION

In the neutron star rest frame (“lab” frame), the electron (positron) is embedded in a radiation field with specific intensity $I_{\epsilon_i}(\hat{\Omega}_i)$. In the electron rest frame, the radiation intensity is

$$I'_{\epsilon'}(\hat{\Omega}') = \left(\frac{\epsilon'}{\epsilon_i} \right)^3 I_{\epsilon_i}(\hat{\Omega}_i), \quad (\text{B1})$$

where ϵ' and ϵ_i are related by a Lorentz transformation: $\epsilon' = \epsilon_i \gamma (1 - \beta \cos \theta_i)$. For a photon coming in along the $\hat{\Omega}'$ direction, the total scattering cross section is $\sigma' = \int d\Omega'_1 \left(\frac{d\sigma}{d\Omega'_1} \right)_{\hat{\Omega}' \rightarrow \hat{\Omega}'_1}$, which in general depends on $\hat{\Omega}'$ and ϵ' . The scattering rate in the electron rest frame is

$$\frac{dN}{dt'} = \int d\Omega' \int d\epsilon' \frac{I'_{\epsilon'}}{\epsilon'} \sigma'. \quad (\text{B2})$$

In the lab frame the scattering rate is $dN/dt = \gamma^{-1} (dN/dt')$ (e.g., Rybicki & Lightman 1979). Using $d\Omega'/d\Omega_i = (\epsilon_i/\epsilon')^2$ and Eq. (B1) we have

$$\frac{dN}{dt} = \int d\Omega_i \int d\epsilon_i (1 - \beta \cos \theta_i) \frac{I_{\epsilon_i}}{\epsilon_i} \sigma'. \quad (\text{B3})$$

Neglecting the angle dependence of σ' and assuming that the radiation field I_{ϵ_i} is isotropic, this becomes

$$\frac{dN}{dt} \simeq c \int d\epsilon_i \frac{dn_{\text{ph}}}{d\epsilon_i} \sigma', \quad (\text{B4})$$

which is the same as Eq. (66).

REFERENCES

- Abrahams A. M., Shapiro S. L., 1991, *ApJ*, 382, 233.
 Arons J., 1981, *ApJ*, 248, 1099.
 Arons J., 2000, in Kramer M., Wex N., Wielebinski N., eds, *Proc. IAU Colloq. 177, Pulsar Astronomy - 2000 and Beyond*. ASP, San Francisco, p.449.
 Arons J., Scharlemann E. T., 1979, *ApJ*, 231, 854.
 Ashcroft N. W., Mermin N. D., 1976, *Solid State Physics*. Saunders College, Philadelphia.
 Backer D. C., 1976, *ApJ*, 209, 895.
 Beloborodov A. M., Thompson C., 2007, *ApJ*, 657, 967.
 Burgay M. et al., 2006, *MNRAS*, 372, 410.
 Burwitz V. et al., 2003, *A&A*, 399, 1109.
 Camilo F. et al., 2006, *Nature*, 442, 892.
 Camilo F., Ransom S. M., Halpern J. P., Reynolds J., 2007, *ApJ*, 666, 93.
 Cheng A. F., Ruderman M. A., 1980, *ApJ*, 235, 576.
 Daugherty J. K., Harding A. K., 1983, *ApJ*, 273, 761.
 Dermer C. D., 1990, *ApJ*, 360, 197.
 Deshpande A. A., Rankin J. M., 1999, *ApJ*, 524, 1008.
 Erber T., 1966, *Rev. Mod. Phys.*, 38, 626..
 Flowers E. G. et al., 1977, *ApJ*, 215, 291.
 Fushiki I., Gudmundsson E. H., Pethick C. J., Yngvason J., 1992, *Ann. Phys.*, 216, 29.
 Gil J., Melikidze G. I., Geppert U., 2003, *A&A*, 407, 315.
 Gil J., Melikidze G. I., Zhang B., 2006, *ApJ*, 650, 1048.
 Goldreich P., Julian W. H., 1969, *ApJ*, 157, 869.
 Gonthier P. L., Harding A. K., Baring M. G., Costello R. M., Mercer C. L., 2000, *ApJ*, 540, 907.
 Harding A. K., Muslimov A. G., 1998, *ApJ*, 508, 328.
 Herold H., 1979, *PRD*, 19, 2868.
 Hibschan J. A., Arons J., 2001, *ApJ*, 554, 624.
 Ho W. C. G., Kaplan D. L., Chang P., van Adelsberg M., Potekhin A. Y., 2007, *MNRAS*, 375, 821.
 Jessner A., Lesch H., Kunzl T., 2001, *MNRAS*, 547, 959.
 Jones P. B., 1985, *MNRAS*, 216, 503.
 Jones P. B., 1986, *MNRAS*, 218, 477.
 Kadomtsev B. B., 1970, *Zh. Eksp. Teor. Fiz.*, 58, 1765 [1970, *Sov. Phys. JETP*, 31, 945].
 Kaspi V. M., Gavriil F. P., 2004, *Nuc. Phys. B Proc. Suppl.*, 132, 456.
 Kaspi V. M., McLaughlin M. A., 2005, *ApJ*, 618, 41.
 Kramer M., Stappers B. W., Jessner A., Lyne A. G., Jordan C. A., 2007, *MNRAS*, 377, 107.
 Lai D., 2001, *Rev. Mod. Phys.*, 73, 629.
 Lai D., Salpeter E. E., Shapiro S. L., 1992, *Phys. Rev. A*, 45, 4832.
 Lai D., Salpeter E. E., 1997, *ApJ*, 491, 270.
 Manchester R. N., Hobbs G. B., Teoh A., Hobbs, M., 2005, *AJ*, 129, 1993.
 Medin Z., Lai D., 2006, *Phys. Rev. A*, 74, 062507 (ML06a).
 Medin Z., Lai D., 2006, *Phys. Rev. A*, 74, 062508 [ML06b].
 Medin Z., Lai D., 2007, *Advances in Space Research*, 40, 1466.
 Melrose D., 2004, in Camilo F., Gaensler B. M., eds, *Proc. IAU Symp. 218, Young Neutron Stars and Their Environments*. ASP, San Francisco, p.349.
 Mori K., Ruderman M., 2003, *ApJ*, 592, L95.
 Müller E., 1984, *A&A*, 130, 415.
 Muslimov A. G., Tsygan A. I., 1992, *MNRAS*, 255, 61.
 Muslimov A. G., Harding A. K., 2003, *ApJ*, 588, 430.
 Muslimov A. G., Harding A. K., 2004, *ApJ*, 606, 1143.
 Neuhauser D., Koonin S. E., Langanke K., 1987, *PRA* 36, 4163.
 Perez-Azorin J. F., Miralles J. A., Pans J. A., 2006, *A&A*, 451, 1009.
 Relovsky B. M., Ruder H., 1996, *PRA*, 53, 4068.
 Ruder H., Wunner G., Herold H., Geyer F., 1994, *Atoms in Strong Magnetic Fields*. Springer-Verlag, Berlin.

- Ruderman M., 1974, in Hansen C. J., ed, Proc. IAU Symp. 53, Physics of Dense Matter. Reidel, Dordrecht-Holland/Boston, p.117.
- Ruderman M., Sutherland P. G., 1975, ApJ, 196, 51.
- Ruderman M., 2003, preprint (astro-ph/0310777).
- Rybicki G. B., Lightman A. P., 1979, Radiative Processes in Astrophysics. Wiley-Interscience, New York.
- Tsong T. T., 1990, Atom-Probe Field Ion Microscopy: Field Ion Emission and Surfaces and Interfaces at Atomic Resolution. Cambridge University, Cambridge.
- Turolla R., Zane S., Drake J. J., 2004, ApJ, 603, 265.
- Usov V. V., Melrose D. B., 1996, ApJ, 464, 306.
- van Adelsberg M., Lai D., Potekhin A. Y., Arras P., 2005, ApJ, 628, 902.
- van Kerkwijk M. H., Kaplan D. L., 2007, Ap&SS, 308, 191.
- Vranevsevic N., Manchester R. N., Melrose D. B., 2006, in Becker W., Huang H. H., eds, Proc. WE-Heraeus Seminar 363, Neutron Stars and Pulsars. MPE Report 291, p.88.
- Weltevrede P., Edwards R. T., Stappers B. W., 2006, ChJAS, 6, 13.
- Woods P. M., Thompson C., 2005, in Lewin W. H. G., van der Klis M., eds, Compact Stellar X-ray Sources. Cambridge University, Cambridge.
- Zhang B., Harding A. K., Muslimov A. G., 2000, ApJ, 531, L135.
- Zhang B., Qiao G. J., Lin W. P., Han J. L., 1997, ApJ, 478, 313.